# Coupled Interactions between Volatile Activity and Fe Oxidation State during Arc Crustal Processes

## M. C. S. Humphreys[1,2]*, R. A. Brooker[3], D. G. Fraser[2], A. Burgisser[4], M. T. Mangan[5] and C. McCammon[6]

[1]Department of Earth Sciences, Durham University, Science Labs, Durham DH1 3LE, UK, [2]Department of Earth Sciences, University of Oxford, South Parks Road, Oxford OX1 3AN, UK, [3]School of Earth Sciences, University of Bristol, Wills Memorial Building, Queen's Road, Bristol BS8 1RJ, UK, [4]CNRS, ISTerre, Universite de Savoie, F-73376 Le Bourget du Lac, France and Université Savoie Mont Blanc, ISTerre, F-73376 Le Bourget du Lac, France, [5]US Geological Survey, 345 Middlefield Road, Menlo Park, CA 94025-3561, USA and [6]Bayerisches Geoinstitut, Universität Bayreuth, D-95440 Bayreuth, Germany

*Corresponding author. Telephone: +44 191 334 2300. Fax: +44 191 334 2301.
E-mail: madeleine.humphreys@durham.ac.uk

## ABSTRACT

Arc magmas erupted at the Earth's surface are commonly more oxidized than those produced at mid-ocean ridges. Possible explanations for this high oxidation state are that the transfer of fluids during the subduction process results in direct oxidation of the sub-arc mantle wedge, or that oxidation is caused by the effect of later crustal processes, including protracted fractionation and degassing of volatile-rich magmas. This study sets out to investigate the effect of disequilibrium crustal processes that may involve coupled changes in $H_2O$ content and Fe oxidation state, by examining the degassing and hydration of sulphur-free rhyolites. We show that experimentally hydrated melts record strong increases in $Fe^{3+}/\sum Fe$ with increasing $H_2O$ concentration as a result of changes in water activity. This is relevant for the passage of $H_2O$-undersaturated melts from the deep crust towards shallow crustal storage regions, and raises the possibility that vertical variations in $fO_2$ might develop within arc crust. Conversely, degassing experiments produce an increase in $Fe^{3+}/\sum Fe$ with decreasing $H_2O$ concentration. In this case the oxidation is explained by loss of $H_2$ as well as $H_2O$ into bubbles during decompression, consistent with thermodynamic modelling, and is relevant for magmas undergoing shallow degassing en route to the surface. We discuss these results in the context of the possible controls on $fO_2$ during the generation, storage and ascent of magmas in arc settings, in particular considering the timescales of equilibration relative to observation as this affects the quality of the petrological record of magmatic $fO_2$.

**Key words**: degassing; hydration; oxidation state; oxygen fugacity; rhyolite; $H_2O$ activity

## INTRODUCTION

A fundamental question in the Earth Sciences concerns the distribution of oxygen within the solid Earth, its cycling through subduction zones and, through volcanic degassing, its effects on the atmosphere. In particular, the controls on the oxidation state of melts as they pass through the mantle and crust are challenging to constrain. It is clear that transfer of hydrous fluids from the subducting slab into the mantle is crucial for generating some of the typical geochemical signatures of subduction zone magmas, such as enrichment in large ion lithophile elements (LILE) and volatiles. Comparison of $Fe^{3+}/\sum Fe$ in lavas arriving at the Earth's surface shows that arc lavas also tend to be more oxidized than

those produced at mid-ocean ridges or in other settings (e.g. Carmichael, 1991; Ballhaus, 1993; Lee *et al.*, 2010; Evans *et al.*, 2012). Mantle xenoliths entrained by arc magmas also appear to be more oxidized than those in other tectonic environments (e.g. Wood *et al.*, 1990; Brandon & Draper, 1996; Parkinson & Arculus, 1999; Frost & McCammon, 2008).

It is commonly suggested that increased $fO_2$ in arc systems compared with other tectonic settings is a primary feature related to mass transfer from the subducting slab to the mantle wedge (e.g. Brandon & Draper, 1996; Parkinson & Arculus, 1999; Kelley & Cottrell, 2009), either directly through addition of volatiles, or indirectly if hydrous fluids carry dissolved $Fe^{3+}$ or sulphate (Kelley & Cottrell, 2009). However, subduction zone magmatism is also characterized by complex crustal processes that could be expected to exert significant controls on oxidation state. These processes include magma fractionation, decompression, degassing and eruption. Arc magmas tend to be volatile rich and may be more prone to stalling and storage in the crust during ascent; this may increase the importance of fractionation and degassing in particular. Arc magmas also tend to crystallize magnetite early during differentiation, and studies based on the partitioning of redox-sensitive incompatible elements suggest that magmatic differentiation could be one reason for the higher $Fe^{3+}/\sum Fe$ of arc lavas (e.g. Mallman & O'Neill, 2009; Lee *et al.*, 2010). Other studies suggest that the influence of volatiles on $fO_2$ could be significant, particularly during crustal processes such as the degassing of C–O–H–S volatile species during shallow magma ascent (e.g. Sato, 1978; Mathez, 1984; Candela, 1986; Burgisser & Scaillet, 2007; Burgisser *et al.*, 2008; Fiege *et al.*, 2014).

Understanding the relationship between volatiles and the oxidation state of magmas involves untangling two distinct problems. The first problem is the fundamental effect of dissolved volatiles, as chemical constituents of the melt, in determining Fe oxidation state. This is at the heart of whether $H_2O$ can itself be an important oxidizing agent, or whether the observed link between $H_2O$ and $Fe^{3+}/\sum Fe$ is possible only by association with oxidized components in slab fluids (e.g. Lecuyer & Ricard, 1999; Parkinson & Arculus, 1999). The second problem is to understand the ways in which crustal processes may affect both melt volatile concentrations and melt oxidation state. These effects include (1) variations in equilibrium volatile speciation and Fe redox state with pressure and temperature, and (2) factors related to processes such as magmatic degassing; these factors could be truly disequilibrium (i.e. kinetically inhibited over the time- and length-scale of interest) or open system (for example, involving segregation of melt and vapour).

In Part I of this study we present a brief review of literature evidence relating to the first problem, that of chemical mechanisms linking volatile dissolution with melt oxidation state, to consider whether volatiles can fundamentally affect oxidation state via melt chemistry.

In Part II, we tackle the second problem, presenting new data to explore the effect of disequilibrium or open-system changes in $H_2O$ content on the oxidation state of sulphur-free rhyolite melts and glasses, using a new series of coupled $H_2O$ and $Fe^{3+}/\sum Fe$ measurements from existing hydration and decompression experiments. We discuss the implications of our results for processes operating in natural magmas, highlighting the need to consider kinetics in arc systems where there is ample evidence of disequilibrium at a variety of temporal and spatial scales.
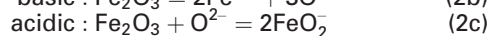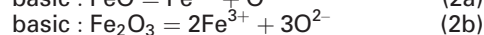
## PART I: A REVIEW OF THE EVIDENCE LINKING VOLATILES, MELT CHEMISTRY AND OXIDATION STATE

The effects of variations in anhydrous melt composition on ferric–ferrous ratios at constant $fO_2$ are well known (e.g. Paul & Douglas, 1965; Sack *et al.*, 1980; Kress & Carmichael, 1991; Toplis, 2005), but there has been considerable debate over the effect of $H_2O$, as a chemical component of the melt, on $Fe^{3+}/\sum Fe$. In particular, it has been suggested that the same process that causes oxidation when alkalis are added to silicate melts at constant $fO_2$ (e.g. Paul & Douglas, 1965) should also operate during dissolution of volatile species (Fraser, 2005; Moretti, 2005; Toplis, 2005), by altering the relative activity coefficients of $Fe^{2+}$ and $Fe^{3+}$ species within the melt.

This relies on the quasi-chemical theory defined by the Lux–Flood 'basicity' of different oxide components, which considers equilibrium between bridging oxygens ($O^0$), non-bridging oxygens ($O^-$) and 'free oxide' anions that are not bonded to the tetrahedral silicate polymer network ($O^{2-}$, Toop & Samis, 1962). In this model, the melt is a molten ionic solution dominated by oxide ions (Flood & Förland, 1947; Fraser, 1975, 2005; Duffy, 1993; Ottonello *et al.*, 2001; Moretti, 2005). Interaction between oxygen in different structural positions

$$O^0 + O^{2-} = 2O^- \qquad (1)$$

defines the basicity of the solution. Basic oxides such as alkalis ($Na_2O$ or $K_2O$) dissociate to supply $O^{2-}$ to the system and hence drive depolymerization [breaking of oxo-bridges; equilibrium (1) moves to the right], whereas acidic oxides (such as $SiO_2$) react with $O^{2-}$ to form polymer chains. Amphoteric oxides, including $Fe_2O_3$, $Al_2O_3$, $H_2O$ and $CO_2$ (Fraser, 1977), can act as an acid or a base depending on the composition of the silicate solution (Kushiro, 1975). Fe oxide components in the silicate melt therefore have the following possible reactions (neglecting the acidic behaviour of FeO; Fraser, 1975, 2005):

$$\text{basic}: FeO = Fe^{2+} + O^{2-} \qquad (2a)$$
$$\text{basic}: Fe_2O_3 = 2Fe^{3+} + 3O^{2-} \qquad (2b)$$
$$\text{acidic}: Fe_2O_3 + O^{2-} = 2FeO_2^- \qquad (2c)$$

where $FeO_2^-$ is part of the structural network, analogous to $AlO_4^-$.

Some evidence suggests that the dissolution of $H_2O$ in polymerized silicate melts occurs by a depolymerization reaction with the tetrahedral network by breaking of T–O–T bridges to form shorter polymer chains terminated by –OH (e.g. Stolper, 1982; Xue & Kanzaki, 2006; Malfait *et al.*, 2014; although also see Kohn, 2000), as well as by incorporation of unreacted molecular $H_2O$ (e.g. Burnham, 1975; Stolper, 1982). This suggests that in these cases, dissolved $H_2O$ should also show basic behaviour, similar to $K_2O$ or $Na_2O$ (in addition to the incorporation of unreacted, molecular water):

$$\text{basic} : H_2O + O^0 = 2OH \qquad (3a)$$
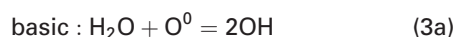
In strongly basic melts, it was predicted that $H_2O$ could also behave as an acidic oxide (Fraser, 1977; Yokokawa, 1986; Fraser, 2005; Moretti, 2005):

$$\text{acidic} : H_2O + O^{2-} = 2OH^- \qquad (3b)$$
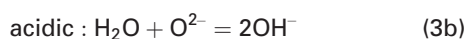
where $OH^-$ is 'free hydroxyl' that is not bound to the silicate network but is complexed with metal cations. This is supported by $^1H$ nuclear magnetic resonance (NMR) experiments (Xue & Kanzaki, 2004) and may contribute to variations in solubility with silicate melt composition (Yokokawa, 1986). Similar reactions are suggested for dissolution of $CO_2$, and this is supported by variations in carbon speciation with melt basicity (Brooker *et al.*, 1999) as well as NMR and Raman spectroscopy studies (Mysen *et al.*, 2011).

## Linking $H_2O$ solubility, melt basicity and oxidation state

In silicate melts, the ratios of multivalent ions such as $Eu^{3+}/Eu^{2+}$ increase with increasing melt basicity ($aO^{2-}$) at constant $fO_2$ (Morris & Haskin, 1974; Tilquin *et al.*, 1997). This is consistent with thermodynamic constraints if the amphoteric behaviour of Fe oxide components is considered [reactions (2a)–(2c); Fraser, 1975], and explains the observed increase of $Fe^{3+}/Fe^{2+}$ with increasing alkali (or basic oxide) content of the melt (e.g. Paul & Douglas, 1965; Sack *et al.*, 1980; Kress & Carmichael, 1991; Toplis, 2005). Increasing the availability of free oxide ($O^{2-}$) leads to an overall net decrease of $aFe_2O_3(m)$ from reactions (2b) and (2c) while simultaneously increasing $aFeO(m)$ from reaction (2a). This produces an overall increase in $Fe^{3+}/\sum Fe$ at constant $fO_2$, and should also polymerize the melt structure, because of the contribution of $FeO_2^-$ to the melt framework (Fraser, 1977, 2005; Ottonello *et al.*, 2001; Moretti, 2005).

For volatiles, the same approach predicts that (basic) reaction of $H_2O$ with the silicate melt to form dissolved $OH^-$ (3a) should result in a net increase in $aO^{2-}$ (and hence increasing $Fe^{3+}/\sum Fe$) whereas (acidic) formation of free hydroxyl in very basic melts (3b) results in a net decrease in $aO^{2-}$ (and hence decreased $Fe^{3+}/\sum Fe$). Similarly, dissolution of carbon dioxide in basic melts should result in a net decrease in $aO^{2-}$, and thus decreasing $Fe^{3+}/\sum Fe$. This provides a testable link

between volatile solution mechanisms and melt oxidation state, which we review below.

## Previous work on $Fe^{3+}/Fe^{2+}$ in hydrous melts

Several previous studies have attempted to discern differences in redox state between equivalent hydrous and anhydrous melt compositions, with somewhat equivocal results. Moore *et al.* (1995) found no effect of $H_2O$ on the Fe oxidation state of hydrous peralkaline rhyolites, supporting an earlier study (Sisson & Grove, 1993) that compared $Fe^{3+}/\sum Fe$ in hydrous basalts with the anhydrous predictions of the Kress & Carmichael (1991) model. Botcharnikov *et al.* (2005) concluded that $Fe^{3+}/\sum Fe$ in hydrous ferrobasalt was mainly controlled experimentally by $aH_2O$ (and hence $fO_2$) and was within the range predicted by existing anhydrous models.

In contrast, Gaillard *et al.* (2001) showed that addition of up to 6 wt % $H_2O$ has an oxidizing effect on metaluminous rhyolite relative to Kress & Carmichael (1991), but only at lower $fO_2$ conditions ($<$NNO + 1, where NNO is nickel–nickel oxide buffer). Gaillard *et al.* (2003b) also observed higher $Fe^{3+}/\sum Fe$ in hydrous vs anhydrous rhyolite and ascribed this to a decrease in the ratio of activity coefficients ($\gamma_{Fe2O3}^L/\gamma_{FeO}^L$) in hydrous melts, or decreasing $a_{Fe2O3}^L$ for a given $XFe_2O_3$ and increasing $a_{FeO}^L$ for a given $XFeO^L$. This is essentially the same effect as predicted by acid–base theory (as described above). Schuessler *et al.* (2008) found that $Fe^{3+}/\sum Fe$ increased with $H_2O$ content at constant $fO_2$ in hydrous phonotephrites, which they attributed to the effects of melt basicity as described by Ottonello *et al.* (2001) and Moretti (2005). These principles are also supported by observations of differences in olivine–melt $K_D^{Fe-Mg}$ in hydrous and anhydrous melts (Toplis, 2005).

Thus, although the results are still unclear, it does seem possible that $H_2O$ has a resolvable effect on melt $Fe^{3+}/\sum Fe$ through behaviour that is similar to that of the basic metal oxides (e.g. $K_2O$). Such an effect is probably minor, but would be most important in relatively polymerized melts and at high pressures where variations in oxidation state could affect the compositions of minerals that could fractionate $Fe^{2+}$ from $Fe^{3+}$. This would appear to justify further work in the context of hydrous subduction zone melts. The basicity approach highlights that oxidation state should be considered alongside an understanding of melt chemical species and melt structure.

## PART II: EFFECT OF VARYING VOLATILE CONTENTS ON OXIDATION STATE

The second part of this study specifically addresses how variations in melt volatile concentrations during crustal processes may affect melt $Fe^{3+}/\sum Fe$. We seek to explore two key processes in particular: (1) dehydration or degassing of volatiles during decompression; (2) hydration owing to $H_2O$-undersaturated magma ascent from high pressures. We present new X-ray absorption near edge structure (XANES) $Fe^{3+}/\sum Fe$ analyses for

two sets of existing experimental samples to investigate these processes: a set of decompression experiments from the study of Mangan & Sisson (2000), and a set of partial hydration experiments from Humphreys *et al.* (2008). A brief description of the experimental procedures is included below.

### Decompression and H$_2$O degassing experiments

Samples of the experimentally degassed Panum Crater Dome obsidian were taken from the study of Mangan & Sisson (2000; Table 1). The starting materials for these experiments were slabs of obsidian, loaded into Pt capsules together with excess H$_2$O. The samples were superheated at 1000°C for several hours in Hf–Zr–Mo cold-seal pressure vessels at 200 MPa, pressurized using Ar gas, then equilibrated at 900°C for 3 days, and finally decompressed isothermally at 0·025 MPa s$^{-1}$ to variable final pressure ($P_f$) and immediately quenched. Decompression runs lasted 17–117 min. There was no attempt to buffer $fO_2$ but rapid H$_2$ diffusion through the Pt capsule would have equilibrated the samples at a high $fO_2$ during the initial 3 day heating. Any observed covariance between H$_2$O loss and Fe$^{3+}$/$\sum$Fe over short lengthscales in the samples must therefore be related to the short decompression phase of the experiment. The resulting glasses are variably vesicular, with bubbles nucleating throughout the capsule in some runs, but only at the margins of the capsule in others (Table 1; Mangan & Sisson, 2000). Most of the samples analysed by XANES contained primarily marginal bubbles. H$_2$O contents and vesicularity data clearly demonstrate that bubble nucleation was delayed and did not occur at equilibrium (Mangan & Sisson, 2000), yielding a suite of glasses with heterogeneous H$_2$O contents over short lengthscales. The anhydrous composition of the glass is constant within analytical uncertainty (Table 2), indicating that no other compositional changes to the melt occurred during degassing.

### Partial hydration experiments

To compare the mechanisms of hydration and H$_2$O degassing, we analysed partially hydrated Lipari obsidian cores as reported by Humphreys *et al.* (2008). The starting materials for these experiments were cylinders of homogeneous Lipari obsidian, which were loaded into gold capsules with excess H$_2$O, along with a small amount of finely ground obsidian powder to prevent dissolution of the glass during the experiment. The capsules were then held at super-liquidus conditions, 150–200 MPa and 855–905°C, in a cold-seal pressure vessel apparatus pressurized by water. Run times were short (20–80 min) and achieved partial hydration of the glass cylinders (Table 1; Humphreys *et al.*, 2008). No double-capsule oxygen buffer control was used during the experiments, but the short run times, low temperatures and use of Au capsules effectively ensure impermeability to H$_2$ during the experiments (Chou, 1986). The anhydrous composition of the glass is constant within analytical uncertainty (Table 2), indicating that

**Table 1**: Experimental details for Panum Dome rhyolite samples from Mangan & Sisson (2000) and for Lipari obsidian from Humphreys et al. (2008). $P_f$, final pressure.

| Sample | d$P$/d$t$ (MPa s$^{-1}$) | $P_f$ (MPa) | Run time (min) | Comments |
|---|---|---|---|---|
| *Panum Dome* | | | | |
| 58 | 0·025 | 25 | 117 | Pervasive bubble cloud |
| 63 | 0·025 | 100 | 67 | Fringe bubbles only |
| 65 | 0·025 | 31 | 113 | Pervasive bubble cloud |
| 68 | 0·025 | 175 | 17 | Fringe bubbles only |
| | $P$ (MPa) | $T$(°C) | Run time (min) | |
| *Lipari* | | | | |
| LIPRF2 | 200 | 857 | 20 | |
| LIPRF3 | 200 | 859 | 80 | |
| LIPRF5 | 150 | 899 | 67 | |
| LIPRF7 | 150 | 901 | 20 | |

hydration is not associated with any other compositional changes to the melt.

## ANALYTICAL METHODS

### X-ray absorption near edge structure (XANES)

Fe$^{3+}$/$\sum$Fe values of experimental glasses were measured using Fe K-edge micro X-ray absorption near edge structure ($\mu$XANES) spectroscopy on the I18 (Microfocus Spectroscopy) beamline at the Diamond Light Source, UK. Spectra were recorded in fluorescence mode and the beam size at the sample was *c.* 3 $\mu$m × 5 $\mu$m. The beamline uses a Si(111) crystal monochromator, which gives an energy resolution ($\Delta E/E$) of 1·4 × 10$^{-4}$ (*c.* 1 eV at the Fe K-edge); the energy stability of the beamline is ±0·05 eV per day. Fluorescence X-rays were normalized to the incident beam flux and collected using a nine-element solid-state detector. The energy was calibrated by defining the first peak of the first derivative of Fe foil to be at 7112 eV (or 7111·1 eV for comparison with older published literature data; e.g. Wilke *et al.*, 2001). Spectra were recorded from 7028 to 7400 eV using a 0·086 eV step over the pre-edge region (7098–7123 eV), 0·259 eV step across the edge (7123–7158 eV) and ∼5 eV step to define both the baseline (7028–7098 eV) and the post-edge region. Initial spectra were collected up to 7340 eV but this was extended to 7400 eV in later runs to aid the normalization procedure (see below). Counting times were 2000 ms on all points. The locations of all points analysed were recorded carefully with reference to reflected light images of the samples to allow accurate relocation for later secondary ion mass spectrometry (SIMS) analyses of the same points.

Fe$^{3+}$/$\sum$Fe measurements were quantified by referencing the centroid energy of the pre-edge feature to a linear calibration (Fig. 1a) constructed using a suite of anhydrous rhyolite glass standards that were synthesized at 1 atm and a range of $fO_2$ (FMQ + 0·8 to FMQ + 6, where FMQ is fayalite–magnetite–quartz buffer) and Fe$^{3+}$/$\sum$Fe from 0·238 to 0·806 (Cottrell *et al.*, 2009;

**Table 2**: Electron microprobe compositions of starting glass and experimental run products, reported on an anhydrous basis

| | Panum Dome (Mangan & Sisson, 2000) | | | Lipari obsidian (Humphreys et al., 2008) | | |
|---|---|---|---|---|---|---|
| | Starting material | Av. run products (anhydrous) | $1\sigma$ | Starting material | Av. run products (anhydrous) | $1\sigma$ |
| $SiO_2$ | 75·64 | 76·94 | 0·52 | 74·17 | 74·39 | 1·6 |
| $TiO_2$ | 0·08 | 0·06 | 0·02 | 0·08 | 0·08 | 0·03 |
| $Al_2O_3$ | 12·38 | 12·56 | 1·05 | 12·76 | 12·95 | 1·08 |
| FeO | 0·94 | 1·01 | 0·26 | 1·57 | 1·59 | 0·45 |
| MnO | 0·07 | 0·05 | 0·11 | 0·05 | 0·07 | 0·11 |
| MgO | 0·03 | 0·03 | 0·05 | 0·04 | 0·04 | 0·01 |
| CaO | 0·54 | 0·54 | 0·13 | 0·74 | 0·75 | 0·12 |
| $Na_2O$ | 4·17 | 3·79 | 0·53 | 4·24 | 4·16 | 0·73 |
| $K_2O$ | 4·72 | 4·94 | 0·59 | 5·39 | 5·49 | 0·65 |
| Cl | 0·06 | 0·07 | 0·03 | 0·32 | 0·31 | 0·04 |
| F | | | | 0·16 | 0·18 | 0·23 |
| $H_2O$ | 0·17 | | | 0·23 | | |
| Total | 98·8 | 99·99 | | 99·75 | 100·01 | |
| n | | 33 | | | 110 | |

$1\sigma$ uncertainties are derived from electron microprobe analysis. *n*, number of analyses.
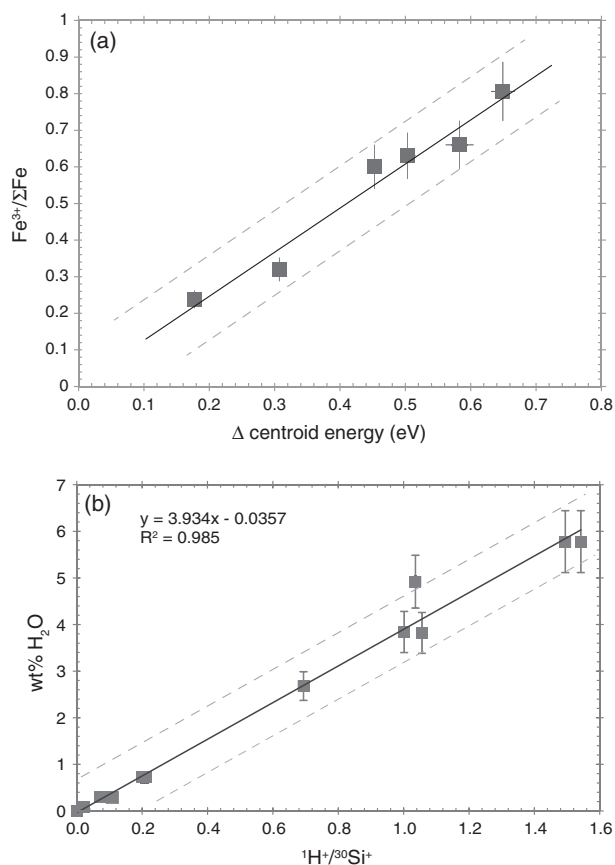


**Fig. 1.** Calibration lines for determining $Fe^{3+}/\sum Fe$ from XANES centroid energy (a) and $H_2O$ from $^1H^+/^{30}Si^+$ ion probe measurements (b). In (a) errors in $Fe^{3+}/\sum Fe$ are derived from Mössbauer spectroscopy (Cottrell et al., 2009), and uncertainties in centroid energy are equivalent to the fitting uncertainty. Data are presented as linear deviation of centroid energy from 7113·6 eV to facilitate regression. Continuous line, best-fit linear regression; dashed lines, fully propagated uncertainties at 80% confidence limits based on the linear regression. (b) Typical daily ion microprobe calibration curve for $^1H^+/^{30}Si^+$ vs $H_2O$ showing best-fit linear regression (continuous line) and upper and lower 95% confidence limits (dashed lines). Uncertainties in $H_2O$ are the errors on independently measured $H_2O$ contents of the standard glasses.

Table 3). The raw spectra were normalized by fitting a straight line to both the low-energy baseline and the post-edge region, using the Athena software package (Ravel & Newville, 2005). The pre-edge feature in Fe spectra typically shows two overlapping peaks whose centroid energy is quantitatively proportional to redox state (e.g. Wilke et al., 2001; Berry et al., 2003; Cottrell et al., 2009). The pre-edge regions of the normalized spectra were fitted between 7106 and ~7118 eV, using a cubic baseline plus a Gaussian to define the rising background towards the main K-edge, and two additional Gaussian peaks to define the pre-edge region (following Berry et al., 2003; Cottrell et al., 2009).

## SIMS and electron microprobe analysis

Glasses were analysed for $^1H^+$, $^7Li^+$, $^{12}C^+$, $^{25}Mg^+/2$, $^{16}O^1H^+$, $^{19}F^+$, $^{23}Na^+$, $^{26}Mg^+$, $^{30}Si^+$, $^{35}Cl^+$ and $^{29}K^+$ using the CAMECA ims 4f secondary ion mass spectrometer at the University of Edinburgh. NIST SRM610 was used as the primary calibration standard; $^{30}Si^+$ was the internal standard. Mass 0·7 was used to monitor the background count rate of the electron multiplier detector. A 10 kV, 2 nA $O^-$ primary beam was accelerated onto the sample with a net impact energy of 14·5 kV. Secondary ions were extracted at +4·5 eV using a 75 V offset. A pre-sputter period of *c.* 2 min, with a nominal 15 μm rastered beam, was used to clean the sample surface, during which time the mass spectrometer was calibrated for the secondary ions. For quantitative analysis, the focused beam was reduced to ~10 μm using a field aperture. $H_2O$ contents of the glass were derived using a daily working curve (Fig. 1b) of measured $^1H^+/^{30}Si^+$ vs $H_2O$ in well-calibrated hydrous glass standards, following the methods of Blundy & Cashman (2005). Typical errors in determining $H_2O$ are ~8–12% relative. Where possible, the same points as analysed by XANES were targeted for SIMS measurements. Major element glass compositions were analysed using a five-spectrometer Cameca SX-100 electron microprobe at the University of Cambridge, with a defocused (15 μm), 15 kV, 4 nA

**Table 3**: XANES fit components, calculated centroid and total intensity for rhyolite standards

| Analysis number | Sample | Fe$^{2+}$ component | | | | | | Fe$^{3+}$ component | | | | | | Centroid (eV) | Total intensity | Fe$^{3+}$/$\sum$Fe |
|---|---|---|---|---|---|---|---|---|---|---|---|---|---|---|---|---|
| | | Fe$^{2+}$ peak location | ± | Width | ± | Intensity | ± | Fe$^{3+}$ peak location | ± | Width | ± | Intensity | ± | | | |
| 8446 | DT31 | 7113·03 | 0·058 | 2·098 | 0·081 | 0·059 | 0·004 | 7114·51 | 0·012 | 1·654 | 0·015 | 0·136 | 0·004 | 7114·12 | 0·194 | 0·63 |
| 8447 | DT18 | 7113·90 | 0·038 | 2·940 | 0·044 | 0·141 | 0·007 | 7114·52 | 0·004 | 1·429 | 0·013 | 0·091 | 0·003 | 7114·20 | 0·232 | 0·66 |
| 8448 | 568_2 | 7112·81 | 0·019 | 1·852 | 0·033 | 0·060 | 0·002 | 7114·47 | 0·011 | 1·622 | 0·020 | 0·077 | 0·002 | 7113·80 | 0·137 | 0·238 |
| 8450 | DT29 | 7113·97 | 0·028 | 2·741 | 0·034 | 0·131 | 0·004 | 7114·53 | 0·005 | 1·448 | 0·016 | 0·097 | 0·003 | 7114·27 | 0·228 | 0·806 |
| 8492 | DT39 | 7112·91 | 0·024 | 1·953 | 0·039 | 0·073 | 0·002 | 7114·50 | 0·009 | 1·571 | 0·016 | 0·110 | 0·002 | 7113·93 | 0·184 | 0·315 |
| 8494 | DT46 | 7113·03 | 0·039 | 2·049 | 0·059 | 0·069 | 0·004 | 7114·50 | 0·009 | 1·554 | 0·012 | 0·139 | 0·003 | 7114·07 | 0·207 | 0·569 |

Fe$^{3+}$/$\sum$Fe values are from Mössbauer spectroscopy (Cottrell et al., 2009).

electron beam for major elements and a 10 nA beam for minor elements. Other analytical conditions were equivalent to those of Humphreys et al. (2006b).

## RESULTS

All the samples studied (including XANES standards) are rhyolite glasses with FeO$_T$ ranging from 1·0 to 5·7 wt %. The resulting XANES spectra show a sharp, clear pre-edge feature, with a well-defined post-edge peak at ∼7130 eV, followed by a deep trough at ∼7160 eV and broad, shallow oscillations in the EXAFS region (Fig. 2). In common with Berry et al. (2003) and Wilke et al. (2005), we observe systematic changes to the shape of the spectra with increasing Fe oxidation state of the standard glasses (Fig. 2), including (1) changes to the shape of the pre-edge feature, (2) an increase in the energy of the main edge, (3) an increase in the height and breadth (and, in detail, a change in the shape) of the post-edge peak, and (4) a slight increase in the energy of the post-edge trough. The change in energy of the post-edge trough has the potential to introduce errors into the dataset during processing if the region ∼7160–7260 eV is used to normalize the spectra. We therefore normalized the spectra to the average intensity of the far post-edge region (up to 7400 eV), which avoids any of these uncertainties. Only the shape of the pre-edge feature was used to make quantitative inferences about the Fe oxidation state of the unknown samples.

The shape of the pre-edge feature is generally quantified by calculating the centroid energy, $C$; that is, the area-weighted average energy of the pre-edge feature:

$$C = E_1 \frac{A_1}{A_1 + A_2} + E_2 \frac{A_2}{A_1 + A_2} \qquad (4)$$

where $E_i$ is the peak energy of component $i$, and $A_i$ is the total area (or integrated intensity) of component $i$. Average precision on the centroid energy from uncertainties in the fitting parameters is extremely good (±0·008 eV) and far better than the accuracy, which relies on calibration of the centroid energy with Fe$^{3+}$/$\sum$Fe. Fully propagated uncertainty for our analyses gave an 80% confidence interval of ∼0·067 for Fe$^{3+}$/$\sum$Fe, but with very high precision. This accuracy translates to $\Delta f$O$_2$ of c. ±0·6 log units. This method

assumes similar Fe coordination in the calibration standards and the unknowns because the intensities of the pre-edge components can vary with both Fe$^{3+}$/$\sum$Fe and iron coordination (Wilke et al., 2001). All our samples have similar total pre-edge intensity (Fig. 3), which suggests no significant change in Fe environment and indicates an average Fe-coordination number of approximately [5], consistent with a stable mixture of [4] and [6] environments (Wilke et al., 2001) for both Fe$^{2+}$ and Fe$^{3+}$. The most oxidized reference glasses plot at slightly higher total intensity than the unknowns, which may be a result of slight self-absorption effects (which has negligible effect on the centroid position; Bajt et al., 1994).

### H$_2$O degassing

The experimentally degassed samples show a range of H$_2$O contents as measured by ion probe and inferred from greyscale variations (Fig. 4). Water contents range from 2·3 to 6·4 wt % H$_2$O, with one measurement at 7·2 wt % H$_2$O (Fig. 4c; Table 4). These values are higher than the volatile contents as measured by Fourier transform infrared (FTIR) spectroscopy (1·8–5·4 wt % H$_2$O; Mangan & Sisson, 2000) but span a similar range. The cause of the discrepancy between the SIMS and FTIR data is unclear; however, the key point for this study is that the glasses show clear relative variations of H$_2$O with Fe$^{3+}$/$\sum$Fe. Back-scattered SEM images of single samples typically show clear increases in greyscale intensity that correlate well with decreasing H$_2$O concentration (Fig. 4b) from the core to the rim of samples with only marginal bubbles. This indicates progressive diffusive loss of H$_2$O to the margins of the sample to feed the growing marginal bubbles. Those samples with more vesicular interiors did not show any clear variations of BSE intensity and typically showed more limited H$_2$O variation.

XANES spectra for these samples have a relatively small range in pre-edge centroid energy from 7114·05 to 7114·15 eV (Table 4). Total pre-edge intensity increases with increasing centroid energy (Fig. 3), consistent with previous observations for silicate glasses (Wilke et al., 2005). The pre-edge centroid energies for these samples correspond to an overall iron oxidation state, Fe$^{3+}$/$\sum$Fe of 0·52–0·64. Although this variation is small compared with the fully propagated
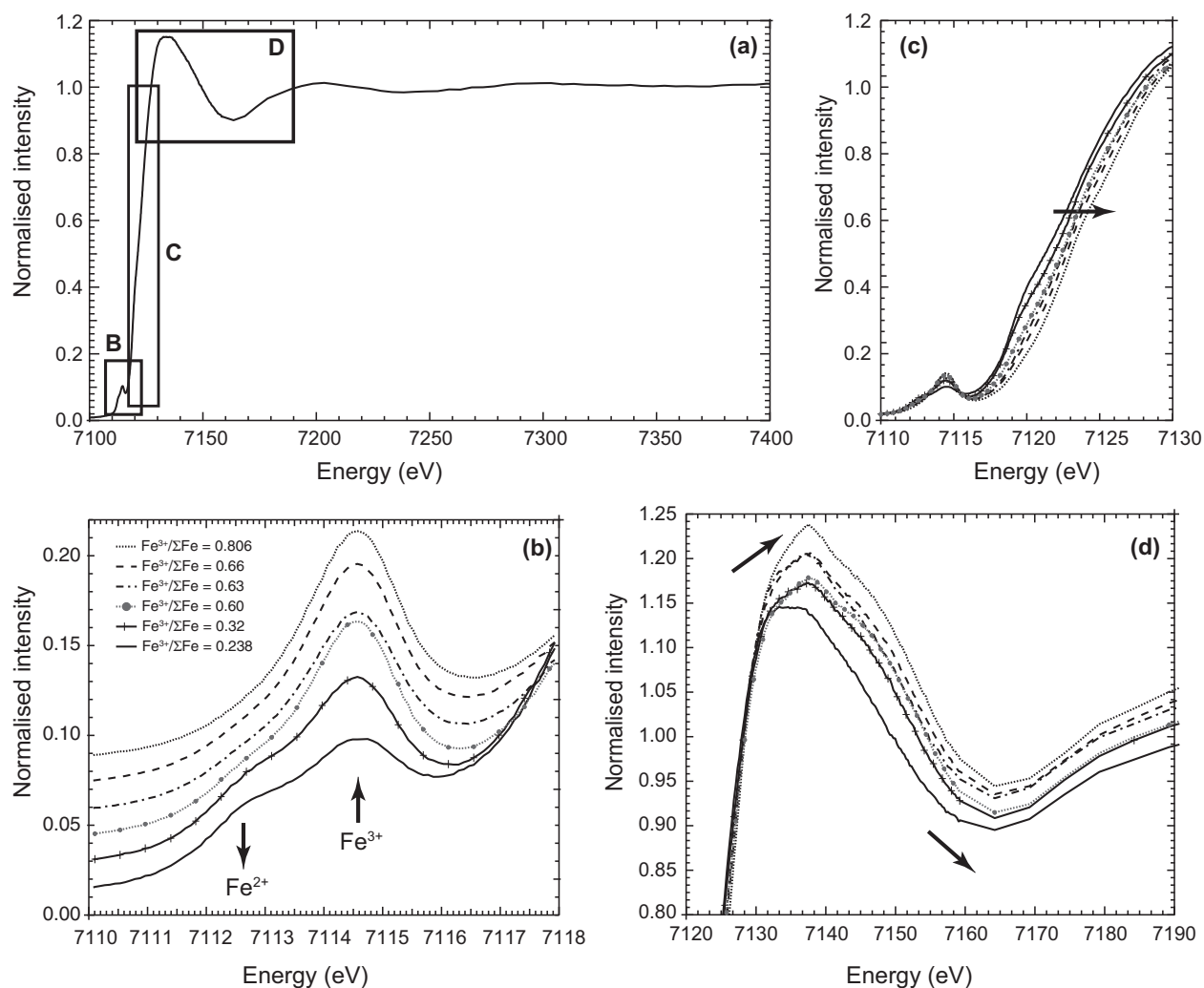
**Fig. 2.** (a) Typical normalized, background-corrected XANES spectrum for rhyolite standard glass. Boxes show parts of the spectrum that show variations with oxidation state. (b) The pre-edge region shows two peaks; the relative importance of the higher-energy peak increases with increasing $Fe^{3+}/\sum Fe$. Each spectrum is offset by 0·02 on the *y*-axis. (c) The energy of the main edge increases systematically with increasing $Fe^{3+}/\sum Fe$ (spectra are not offset). (d) The energy of the peak and post-edge trough increases with $Fe^{3+}/\sum Fe$, although higher energy resolution in this region is needed to use this feature quantitatively. Each spectrum is offset by 0·02 on the *y*-axis. It should be noted that where additional symbol markers are used, these represent every fifth data point.

measurement uncertainty, there are clear relative variations both between and within samples. There is a correlation between $H_2O$ concentration and oxidation state, consistent with an increase in $Fe^{3+}/\sum Fe$ owing to degassing of $H_2O$ from the melt.

## Hydration

The margins of the Lipari obsidian samples are strongly hydrated, with water contents approaching the equilibrium values calculated for the experimental run conditions (4·8–5·6 wt %; Humphreys *et al.*, 2008), whereas the interiors remain unhydrated and record the initial volatile content of the Lipari obsidian starting material (~0·2 wt % $H_2O$; Table 5). The variation in $H_2O$ contents is clearly visible as a strong outward decrease in backscattered SEM intensity (e.g. Fig. 5a; Humphreys *et al.*, 2008). The influx of water into the samples was

previously modelled successfully based on established concentration-dependent $H_2O$ diffusivity data (Nowak & Behrens, 1997; Zhang & Behrens, 2000) and is consistent with $H_2O$ diffusion into the samples over the timescale of the experiments (Humphreys *et al.*, 2008).

XANES spectra for the high-temperature hydrated samples show strong changes in pre-edge centroid energy from 7113·65 to 7114·1 eV, with one outlier at 7113·60 eV (Table 5), corresponding to $Fe^{3+}/\sum Fe$ values from 0·04 to 0·60 (Fig. 5b). In marked contrast to the degassed samples, $H_2O$ concentration correlates positively with oxidation state, indicating increasing $Fe^{3+}/\sum Fe$ linked to diffusion of $H_2O$ into the sample. This is further demonstrated by the close correspondence in the shapes of the compositional profiles with distance from the margin of each chip (Fig. 6). These spatial profiles also highlight a small but apparently significant (in
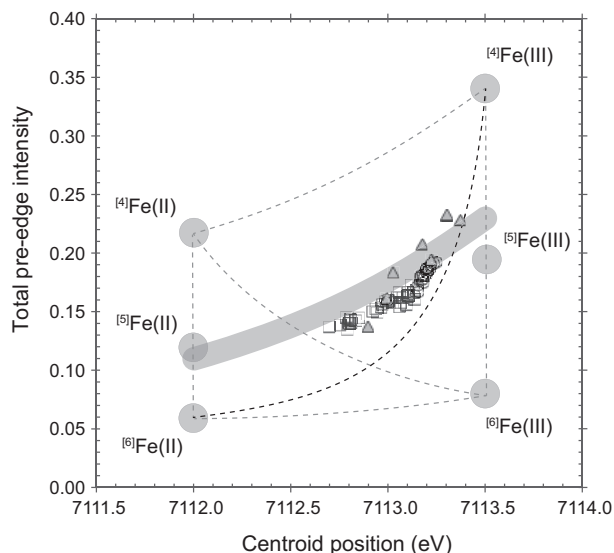
**Fig. 3.** Total pre-edge intensity plotted against pre-edge centroid energy, after Wilke *et al.* (2005). Light grey circles and dashed curves represent Fe coordination end-member positions and mixing lines derived from Wilke *et al.* (2005). Triangles, rhyolite glass standards (Cottrell *et al.*, 2009); squares, partially hydrated Lipari rhyolite; circles, high-temperature degassed rhyolites from Mangan & Sisson (2000). Continuous grey curve represents the range of standard glasses presented by Wilke *et al.* (2005).

that it is present in each sample) negative deviation of $Fe^{3+}/\sum Fe$ at low $H_2O$ contents ($\sim 0.5$–$1.5$ wt % $H_2O$).

## INTERPRETATION

### Oxidation owing to melt hydration

The hydrated samples show clearly that increasing $H_2O$ content causes an increase in the Fe oxidation state (Figs 5 and 6). This observation is very similar to the results of an earlier equilibrium study (Botcharnikov *et al.*, 2005), which used long run times and an AuPd capsule that is permeable to $H_2$ to control $fO_2$ in the experiments, according to the equilibrium constant for the dissociation reaction

$$H_2O(g) = H_2(g) + \tfrac{1}{2}O_2(g) \tag{5}$$
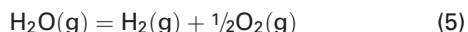
$$K_{eq}^{fl} = (fH_2 \cdot fO_2^{1/2})/fH_2O^{fl}. \tag{6}$$

Although $fH_2$ of the fluid was fixed (via a Shaw membrane), variations of $XH_2O^{fl}$ between capsules introduced differences in equilibrium $fO_2$ in different experimental runs (Botcharnikov *et al.*, 2005), because $fH_2O = aH_2O \times f^0H_2O$ (and assuming ideal behaviour, $aH_2O \sim XH_2O$). The actual $fO_2$ experienced was calculated from the imposed $fO_2$ and $XH_2O$ (Botcharnikov *et al.*, 2005):

$$\log fO_2(\text{actual}) = \log fO_2(\text{imposed}) + 2\log XH_2O. \tag{7}$$

In our experiments, we assume that the use of an Au capsule (minimally permeable to $H_2$ at our experimental temperatures; Chou, 1986) and very short run times (20–80 min) resulted in approximately constant $fH_2$ fluid

inside the experiments (see below). Our experiments were not equilibrated, and diffusion of $H_2O$ from the fluid into the melt resulted in wide variations of $XH_2O$ within each quenched glass chip, from water-saturated at the hydrated margin ($\sim 5.5$–$6$ wt % $H_2O$) to highly undersaturated in the unhydrated core ($\sim 0.2$ wt % $H_2O$). We can write equivalent reactions to (5) and (6) that apply for the melt phase, even though equilibration was incomplete. We therefore calculated the apparent change in log $fO_2$ (melt) following the approach of Botcharnikov *et al.* (2005). We assumed constant $fH_2$, and used either $H_2O_t$ (the total amount of $H_2O$ dissolved in the melt) or the molecular $H_2O_m$ [estimated from Silver *et al.* (1990)] to calculate log $XH_2O_t$ or log $XH_2O_m$; that is, $XH_2O_t = H_2O_t/H_2O_{sat}$ and $XH_2O_m = H_2O_m/H_2O_{sat}$. We also assumed that the marginal glass is $H_2O$-saturated (i.e. that $XH_2O_t = 1$ at the rim), as the rim $H_2O_t$ concentrations agree with solubility models (Humphreys *et al.*, 2008). Calculated $fO_2$ was converted to $Fe^{3+}/\sum Fe$ using the anhydrous algorithm of Kress & Carmichael (1991) for the major element composition of the sample and known experimental conditions. Using this approach, the overall change in $Fe^{3+}/\sum Fe$ from core to rim in the glass samples is matched by the predictions based on observed changes in $XH_2O$ (Fig. 7). The lengthscale of the changes in $Fe^{3+}/\sum Fe$ is also equivalent to the lengthscale of $H_2O$ diffusion gradients, modelled using existing $H_2O_m$ diffusivity data (Humphreys *et al.*, 2008), demonstrating that $Fe^{3+}/\sum Fe$ varies at a rate controlled largely by the diffusivity of $H_2O_m$ (Fig. 6). This implies that Fe oxidation state is dominated by variations in $XH_2O$ during hydration.

However, the shapes of the $H_2O$–$Fe^{3+}/\sum Fe$ profiles do not fit well to the modelled trend (Fig. 7), which suggests that Fe oxidation state was only partly controlled by the disequilibrium changes in $XH_2O$. In particular, there is a significant deviation from the modelled curve to lower $Fe^{3+}$ at low to intermediate water contents (Fig. 7). This is in contrast to equilibrium data (Botcharnikov *et al.*, 2005), which fit the model well (Fig. 7). The discrepancy with the equilibrium data cannot be explained by significant changes in average melt Fe coordination, because the overall intensity of the pre-edge region does not vary significantly with oxidation state (see Fig. 3; although this does not preclude that coordination changes might occur).

Another possibility is that some 'significant' diffusion of $H_2$ did occur across the Au capsule during the course of even these short experiments. As the experiments were unbuffered it is difficult to quantify these effects but we note that any $H_2$ loss from the capsule fluid would result in anomalously oxidized sample margins, whereas $H_2$ gain would result in anomalously reduced sample margins, relative to predicted values. Instead, $Fe^{3+}/\sum Fe$ at the sample margins is well matched by the predictions, whereas the unhydrated cores of the chips are anomalously reduced relative to the predicted curves (Fig. 7). Furthermore, there is no difference in profile shape between the shortest (20 min) and longest
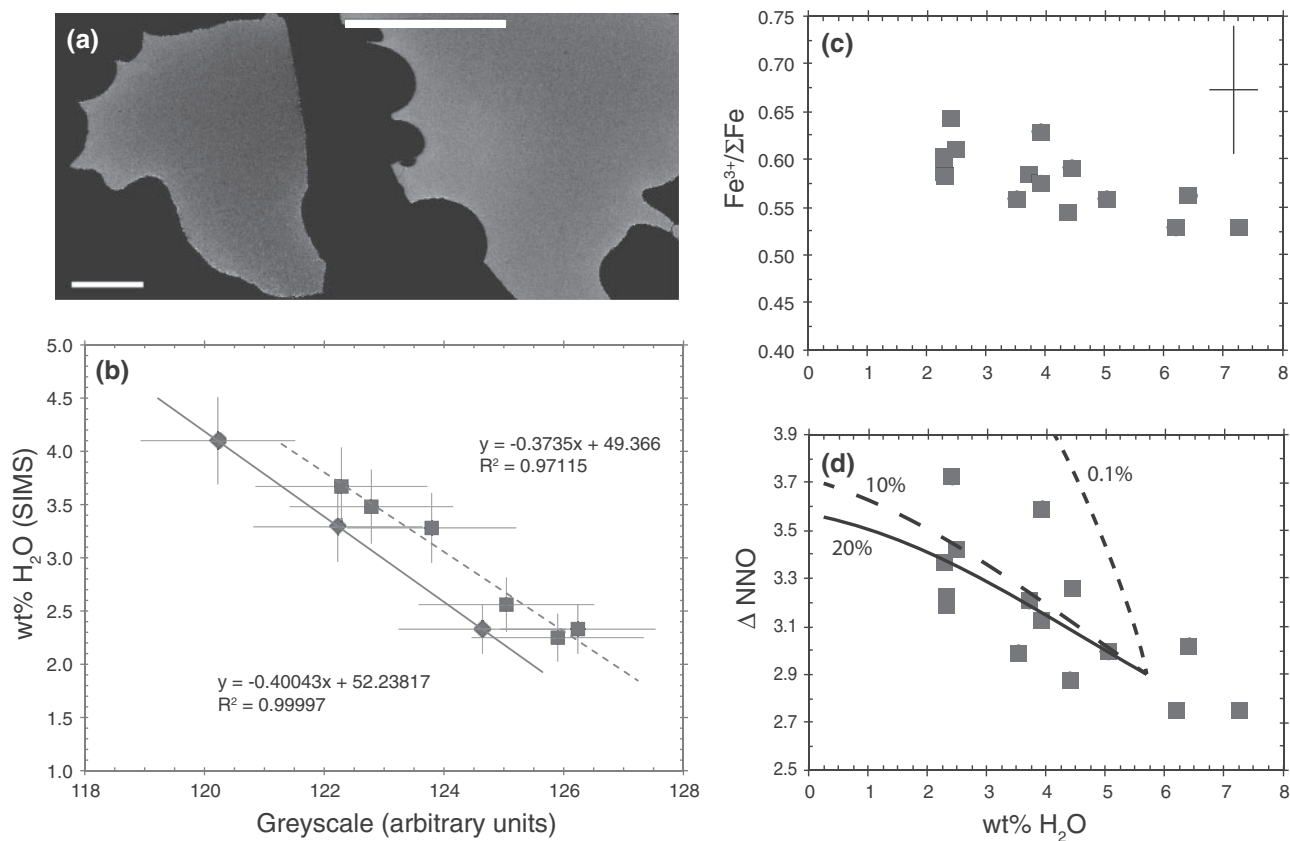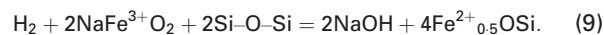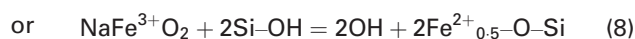
**Fig. 4.** (a) Backscattered electron SEM images of representative glass chips from Mangan & Sisson (2000), in which heterogeneous bubble nucleation at the margins of the chips was dominant. Scale bar represents 1 mm. Lower greyscale intensity in the core indicates higher water contents, as demonstrated by the negative linear correlation between greyscale and $H_2O$ (b). Degassing of $H_2O$ is associated with increasing $Fe^{3+}/\sum Fe$ (c) and $fO_2$ relative to the nickel–nickel oxide buffer (d). Errors in (c) relate to ~10% uncertainty in $H_2O$ and 80% confidence limits for $Fe^{3+}/\sum Fe$. It should be noted that the analytical precision is smaller than the size of the points. Modelled trends in (d) are theoretical predictions for degassing of S-free rhyolite following Burgisser *et al.* (2008), starting with no free fluid (0·1 wt% initial gas, dotted line) or with 10 wt % (dashed line) or 20 wt % (continuous line) initial fluid.

experiment (117 min), which supports our interpretation that the experiments approximately represent a closed system. There is also no difference in the width of the low-$Fe^{3+}$ region between the shortest and longest experimental runs (Fig. 6). This suggests that rapid migration of $H_2$ preceding the $H_2O$ diffusion front at high temperature cannot explain the discrepancy between model and observations (see Gaillard *et al.*, 2002, 2003c).

Our best explanation is therefore that, although the interconversion reaction between $H_2O$ and OH in the silicate melt is rapid at experimental temperatures (Zhang *et al.*, 1991), reactions involving the Fe species are slower, or may involve intermediate reactions, at low $H_2O$ contents where the melt viscosity is higher. The effect of this would be that any change in $Fe^{3+}/\sum Fe$ is offset to higher $XH_2O$ in these disequilibrium experiments. This could also explain why the longer duration, equilibrium experiments of Botcharnikov *et al.* (2005) are more consistent with the shape of the modelled curves (see Fig. 7). This interpretation is consistent with the observations that relatively slow redox equilibration in metaluminous rhyolites may be linked to intermediate changes in

complexing of network-modifying cations (Gaillard *et al.*, 2003a), such as

or
$$NaFe^{3+}O_2 + 2Si-OH = 2OH + 2Fe^{2+}_{0.5}-O-Si \quad (8)$$
$$H_2 + 2NaFe^{3+}O_2 + 2Si-O-Si = 2NaOH + 4Fe^{2+}_{0.5}OSi. \quad (9)$$

This emphasizes that changes in melt oxidation state are closely linked to variations in melt chemistry and structure. Melt basicity theory may be a useful additional tool for investigation of these sorts of coupled changes than simply $fO_2$ measured relative to traditional oxygen buffers.

## Oxidation owing to $H_2O$ degassing

The data from the experimentally degassed rhyolites are scattered but show a general trend of oxidation by ~0·5–1 log unit $fO_2$ ($Fe^{3+}/\sum Fe$ varies from 0·53 to 0·65) as $H_2O$ contents decrease from ~7 to ~2 wt % (Fig. 4c; Table 4). During decompression, the melt became $H_2O$-saturated and nucleated bubbles of a free $H_2O$ vapour phase. We infer that subsequent re-equilibration of $fH_2$ and $fH_2O$ in the vapour bubble occurred through

**Table 4:** XANES fit components, calculated centroid and total intensity, and calculated $Fe^{3+}/\sum Fe$ for the high-T decompression samples

| Analysis number | Sample | $Fe^{2+}$ component | | | | | | $Fe^{3+}$ component | | | | | | Centroid (eV) | Total intensity | $Fe^{3+}/\sum Fe$ | $H_2O$ (wt %) | ΔNNO | ± |
|---|---|---|---|---|---|---|---|---|---|---|---|---|---|---|---|---|---|---|---|
| | | $Fe^{2+}$ peak location | ± | Width | ± | Intensity | ± | $Fe^{3+}$ peak location | ± | Width | ± | Intensity | ± | | | | | | |
| 8452 | 68-3 | 7112·78 | 0·044 | 1·886 | 0·066 | 0·043 | 0·003 | 7114·42 | 0·013 | 1·74 | 0·018 | 0·124 | 0·002 | 7114·05 | 0·167 | 0·529 | 7·27 | 2·7 | 0·55 |
| 8453 | 68-1 | 7112·74 | 0·035 | 1·840 | 0·055 | 0·043 | 0·002 | 7114·41 | 0·010 | 1·77 | 0·016 | 0·129 | 0·002 | 7114·05 | 0·172 | 0·529 | 6·20 | 2·8 | 0·55 |
| 8454 | 68-2 | 7112·75 | 0·040 | 1·808 | 0·063 | 0·041 | 0·003 | 7114·41 | 0·011 | 1·75 | 0·017 | 0·134 | 0·002 | 7114·08 | 0·175 | 0·562 | 6·42 | 3·0 | 0·57 |
| 8455 | 65-1 | 7112·93 | 0·067 | 1·983 | 0·093 | 0·047 | 0·004 | 7114·46 | 0·014 | 1·70 | 0·017 | 0·145 | 0·004 | 7114·15 | 0·192 | 0·643 | 2·41 | 3·7 | 0·69 |
| 8456 | 65-3 | 7112·85 | 0·051 | 1·915 | 0·076 | 0·046 | 0·003 | 7114·44 | 0·012 | 1·68 | 0·016 | 0·137 | 0·003 | 7114·10 | 0·183 | 0·585 | 3·72 | 3·2 | 0·60 |
| 8457 | 65-3A | 7112·80 | 0·050 | 1·861 | 0·077 | 0·043 | 0·003 | 7114·42 | 0·013 | 1·70 | 0·018 | 0·138 | 0·003 | 7114·09 | 0·181 | 0·575 | 3·92 | 3·1 | 0·59 |
| 8458 | 65-5A | 7113·00 | 0·076 | 2·089 | 0·103 | 0·053 | 0·005 | 7114·47 | 0·015 | 1·67 | 0·017 | 0·137 | 0·004 | 7114·12 | 0·190 | 0·610 | 2·49 | 3·4 | 0·63 |
| 8459 | 65-7 | 7112·81 | 0·050 | 1·907 | 0·075 | 0·046 | 0·003 | 7114·42 | 0·013 | 1·70 | 0·018 | 0·134 | 0·003 | 7114·07 | 0·180 | 0·545 | 4·38 | 2·9 | 0·56 |
| 8460 | 65-9 | 7112·92 | 0·085 | 1·976 | 0·119 | 0·047 | 0·005 | 7114·45 | 0·018 | 1·69 | 0·021 | 0·144 | 0·005 | 7114·14 | 0·191 | 0·629 | 3·92 | 3·6 | 0·66 |
| 8461 | 65-8 | 7112·87 | 0·052 | 1·982 | 0·077 | 0·049 | 0·004 | 7114·44 | 0·012 | 1·68 | 0·016 | 0·133 | 0·003 | 7114·08 | 0·181 | 0·558 | 3·52 | 3·0 | 0·57 |
| 8462 | 58-3 | 7112·96 | 0·054 | 2·059 | 0·076 | 0·053 | 0·004 | 7114·47 | 0·012 | 1·67 | 0·014 | 0·134 | 0·003 | 7114·10 | 0·187 | 0·586 | 2·30 | 3·2 | 0·60 |
| 8463 | 58-2 | 7112·94 | 0·053 | 2·025 | 0·074 | 0·052 | 0·004 | 7114·46 | 0·012 | 1·68 | 0·014 | 0·135 | 0·003 | 7114·10 | 0·186 | 0·583 | 2·31 | 3·2 | 0·60 |
| 8464 | 58-1 | 7112·93 | 0·053 | 1·971 | 0·076 | 0·049 | 0·004 | 7114·46 | 0·012 | 1·68 | 0·015 | 0·137 | 0·003 | 7114·12 | 0·186 | 0·603 | 2·29 | 3·4 | 0·62 |
| 8465 | 63-1 | 7112·83 | 0·047 | 1·913 | 0·070 | 0·044 | 0·003 | 7114·43 | 0·011 | 1·71 | 0·015 | 0·140 | 0·003 | 7114·11 | 0·185 | 0·591 | 4·45 | 3·3 | 0·61 |
| 8466 | 63-3 | 7112·74 | 0·038 | 1·806 | 0·060 | 0·041 | 0·003 | 7114·40 | 0·010 | 1·74 | 0·016 | 0·136 | 0·002 | 7114·08 | 0·177 | 0·559 | 5·04 | 3·0 | 0·57 |

$H_2O$ contents are measured from SIMS. ΔNNO is calculated for 900°C.

**Table 5:** XANES fit components, calculated centroid and total intensity, and calculated $Fe^{3+}/\Sigma Fe$ for the high-T hydration samples

| Analysis number | Sample | $Fe^{2+}$ component | | | | | | $Fe^{3+}$ component | | | | | | Centroid (eV) | Total intensity | Distance from rim (µm) | $Fe^{3+}/\Sigma Fe$ | $H_2O$ (wt %) (SIMS) |
|---|---|---|---|---|---|---|---|---|---|---|---|---|---|---|---|---|---|---|
| | | $Fe^{2+}$ peak location | ± | Width | ± | Intensity | ± | $Fe^{3+}$ peak location | ± | Width | ± | Intensity | ± | | | | | |
| 7272 | LIRPF5-1 | 7112.83 | 0.0285 | 1.7839 | 0.0494 | 0.0416 | 0.0020 | 7114.55 | 0.0078 | 1.722 | 0.013 | 0.139 | 0.002 | 7114.11 | 0.181 | 0 | 0.60 | 5.44 |
| 7273 | LIRPF5-2 | 7112.87 | 0.0303 | 1.8349 | 0.0521 | 0.0479 | 0.0023 | 7114.57 | 0.0099 | 1.687 | 0.017 | 0.120 | 0.002 | 7114.04 | 0.168 | 136 | 0.52 | 5.00 |
| 7274 | LIRPF5-3 | 7112.85 | 0.0259 | 1.8216 | 0.0454 | 0.0498 | 0.0021 | 7114.57 | 0.0094 | 1.696 | 0.017 | 0.113 | 0.002 | 7114.01 | 0.163 | 274 | 0.47 | 4.80 |
| 7275 | LIRPF5-4 | 7112.8 | 0.0207 | 1.7912 | 0.0363 | 0.0510 | 0.0018 | 7114.53 | 0.0083 | 1.714 | 0.016 | 0.111 | 0.002 | 7113.95 | 0.162 | 387 | 0.40 | 4.10 |
| 7276 | LIRPF5-5 | 7112.81 | 0.0209 | 1.8227 | 0.0371 | 0.0551 | 0.0019 | 7114.54 | 0.0091 | 1.694 | 0.018 | 0.104 | 0.002 | 7113.90 | 0.159 | 482 | 0.34 | 3.50 |
| 7277 | LIRPF5-6 | 7112.82 | 0.0187 | 1.7890 | 0.0329 | 0.0572 | 0.0018 | 7114.55 | 0.0093 | 1.698 | 0.020 | 0.096 | 0.002 | 7113.86 | 0.153 | 561 | 0.30 | 2.60 |
| 7278 | LIRPF5-7 | 7112.85 | 0.0170 | 1.8093 | 0.0308 | 0.0673 | 0.0019 | 7114.56 | 0.0119 | 1.632 | 0.025 | 0.073 | 0.002 | 7113.70 | 0.140 | 638 | 0.10 | 1.50 |
| 7279 | LIRPF5-8 | 7112.8 | 0.0144 | 1.7891 | 0.0255 | 0.0701 | 0.0016 | 7114.52 | 0.0115 | 1.650 | 0.028 | 0.067 | 0.002 | 7113.60 | 0.137 | 708 | −0.02 | 0.40 |
| 7280 | LIRPF5-9 | 7112.82 | 0.0175 | 1.7884 | 0.0308 | 0.0658 | 0.0019 | 7114.54 | 0.0117 | 1.667 | 0.027 | 0.077 | 0.002 | 7113.71 | 0.143 | 778 | 0.11 | 0.25 |
| 7281 | LIRPF7-1 | 7112.82 | 0.0365 | 1.8057 | 0.0625 | 0.0437 | 0.0026 | 7114.55 | 0.0125 | 1.752 | 0.022 | 0.117 | 0.002 | 7114.04 | 0.160 | 0 | 0.51 | 5.20 |
| 7282 | LIRPF7-2 | 7112.81 | 0.0277 | 1.8060 | 0.0480 | 0.0480 | 0.0022 | 7114.54 | 0.0099 | 1.724 | 0.018 | 0.118 | 0.002 | 7114.00 | 0.167 | 86 | 0.46 | 4.70 |
| 7283 | LIRPF7-3 | 7112.8 | 0.0230 | 1.8522 | 0.0404 | 0.0519 | 0.0019 | 7114.54 | 0.0086 | 1.716 | 0.015 | 0.115 | 0.002 | 7113.96 | 0.167 | 171 | 0.41 | 3.90 |
| 7284 | LIRPF7-4 | 7112.84 | 0.0211 | 1.8498 | 0.0371 | 0.0572 | 0.0019 | 7114.56 | 0.0092 | 1.684 | 0.017 | 0.102 | 0.002 | 7113.90 | 0.160 | 252 | 0.35 | 2.10 |
| 7285 | LIRPF7-5 | 7112.87 | 0.0150 | 1.8345 | 0.0271 | 0.0686 | 0.0017 | 7114.58 | 0.0103 | 1.621 | 0.022 | 0.071 | 0.002 | 7113.70 | 0.140 | 329 | 0.10 | 0.50 |
| 7286 | LIRPF7-6 | 7112.84 | 0.0171 | 1.8011 | 0.0301 | 0.0649 | 0.0018 | 7114.56 | 0.0108 | 1.664 | 0.024 | 0.080 | 0.002 | 7113.75 | 0.145 | 394 | 0.16 | 0.20 |
| 4660 | LIRPF2-1 | 7112.72 | 0.0231 | 1.7718 | 0.0412 | 0.0431 | 0.0017 | 7114.51 | 0.0087 | 1.787 | 0.018 | 0.111 | 0.002 | 7113.96 | 0.154 | 0 | 0.41 | 6.10 |
| 4662 | LIRPF2-2 | 7112.88 | 0.0327 | 1.8514 | 0.0556 | 0.0472 | 0.0025 | 7114.57 | 0.0120 | 1.737 | 0.021 | 0.108 | 0.002 | 7114.00 | 0.156 | 61 | 0.46 | 5.80 |
| 4663 | LIRPF2-3 | 7112.83 | 0.0240 | 1.8290 | 0.0419 | 0.0502 | 0.0020 | 7114.57 | 0.0094 | 1.723 | 0.018 | 0.107 | 0.002 | 7113.97 | 0.157 | 125 | 0.42 | 5.00 |
| 4664 | LIRPF2-4 | 7112.78 | 0.0213 | 1.8283 | 0.0369 | 0.0537 | 0.0018 | 7114.52 | 0.0093 | 1.728 | 0.019 | 0.102 | 0.002 | 7113.87 | 0.156 | 199 | 0.31 | 3.50 |
| 4670 | LIRPF2-5 | 7112.84 | 0.0248 | 1.8271 | 0.0434 | 0.0582 | 0.0023 | 7114.57 | 0.0126 | 1.690 | 0.026 | 0.091 | 0.003 | 7113.84 | 0.149 | 225 | 0.27 | 2.90 |
| 4665 | LIRPF2-6 | 7112.76 | 0.0176 | 1.7885 | 0.0314 | 0.0628 | 0.0018 | 7114.49 | 0.0117 | 1.668 | 0.026 | 0.076 | 0.002 | 7113.65 | 0.138 | 244 | 0.04 | 1.50 |
| 4666 | LIRPF2-7 | 7112.8 | 0.0167 | 1.8094 | 0.0299 | 0.0667 | 0.0018 | 7114.53 | 0.0108 | 1.663 | 0.025 | 0.079 | 0.002 | 7113.69 | 0.145 | 303 | 0.08 | 0.40 |
| 4667 | LIRPF2-8 | 7112.82 | 0.0199 | 1.7933 | 0.0354 | 0.0649 | 0.0021 | 7114.54 | 0.0132 | 1.665 | 0.029 | 0.077 | 0.002 | 7113.70 | 0.142 | 398 | 0.10 | 0.20 |
| 4668 | LIRPF2-9 | 7112.88 | 0.0161 | 1.8471 | 0.0288 | 0.0671 | 0.0017 | 7114.59 | 0.0103 | 1.642 | 0.022 | 0.075 | 0.002 | 7113.73 | 0.142 | 474 | 0.14 | 0.20 |
| 4671 | LIRPF3-1 | 7112.86 | 0.0410 | 1.8802 | 0.0669 | 0.0447 | 0.0028 | 7114.54 | 0.0111 | 1.714 | 0.017 | 0.133 | 0.002 | 7114.07 | 0.178 | 0 | 0.54 | 5.40 |
| 4672 | LIRPF3-2 | 7112.83 | 0.0361 | 1.8774 | 0.0600 | 0.0469 | 0.0026 | 7114.53 | 0.0108 | 1.722 | 0.018 | 0.126 | 0.002 | 7114.02 | 0.173 | 34 | 0.49 | 5.40 |
| 4673 | LIRPF3-3 | 7112.81 | 0.0289 | 1.7642 | 0.0493 | 0.0433 | 0.0021 | 7114.53 | 0.0096 | 1.744 | 0.018 | 0.123 | 0.002 | 7114.03 | 0.166 | 78 | 0.50 | 5.30 |
| 4674 | LIRPF3-4 | 7112.85 | 0.0299 | 1.8570 | 0.0514 | 0.0492 | 0.0023 | 7114.57 | 0.0104 | 1.706 | 0.018 | 0.114 | 0.002 | 7114.00 | 0.163 | 136 | 0.46 | 5.00 |
| 4675 | LIRPF3-5 | 7112.85 | 0.0280 | 1.8431 | 0.0486 | 0.0497 | 0.0023 | 7114.58 | 0.0102 | 1.720 | 0.018 | 0.114 | 0.002 | 7114.01 | 0.164 | 171 | 0.47 | 4.80 |
| 4676 | LIRPF3-6 | 7112.83 | 0.0277 | 1.8342 | 0.0491 | 0.0505 | 0.0023 | 7114.57 | 0.0105 | 1.711 | 0.019 | 0.111 | 0.002 | 7113.98 | 0.162 | 225 | 0.43 | 4.70 |
| 4677 | LIRPF3-7 | 7112.83 | 0.0288 | 1.8502 | 0.0504 | 0.0521 | 0.0024 | 7114.54 | 0.0112 | 1.685 | 0.020 | 0.105 | 0.002 | 7113.92 | 0.158 | 281 | 0.37 | 4.70 |
| 4678 | LIRPF3-8 | 7112.74 | 0.0263 | 1.7600 | 0.0472 | 0.0507 | 0.0023 | 7114.5 | 0.0112 | 1.729 | 0.024 | 0.108 | 0.002 | 7113.89 | 0.159 | 326 | 0.33 | 4.40 |
| 4679 | LIRPF3-9 | 7112.78 | 0.0196 | 1.7886 | 0.0349 | 0.0548 | 0.0018 | 7114.51 | 0.0094 | 1.700 | 0.019 | 0.097 | 0.002 | 7113.84 | 0.152 | 367 | 0.27 | 4.40 |
| 4680 | LIRPF3-10 | 7112.81 | 0.0239 | 1.8159 | 0.0407 | 0.0575 | 0.0022 | 7114.53 | 0.0123 | 1.709 | 0.025 | 0.092 | 0.002 | 7113.82 | 0.150 | 404 | 0.25 | 4.00 |
| 4681 | LIRPF3-11 | 7112.81 | 0.0156 | 1.7353 | 0.0271 | 0.0617 | 0.0016 | 7114.53 | 0.0114 | 1.698 | 0.027 | 0.073 | 0.002 | 7113.69 | 0.135 | 454 | 0.09 | 3.60 |
| 4682 | LIRPF3-12 | 7112.83 | 0.0161 | 1.7828 | 0.0293 | 0.0647 | 0.0017 | 7114.56 | 0.0108 | 1.647 | 0.024 | 0.075 | 0.002 | 7113.71 | 0.140 | 633 | 0.11 | 0.90 |
| 7287 | Starting material | 7112.81 | 0.0155 | 1.7998 | 0.0274 | 0.0657 | 0.0017 | 7114.54 | 0.0103 | 1.669 | 0.023 | 0.077 | 0.002 | 7113.70 | 0.143 | | 0.10 | 0.23 |

$H_2O$ contents are measured from SIMS.
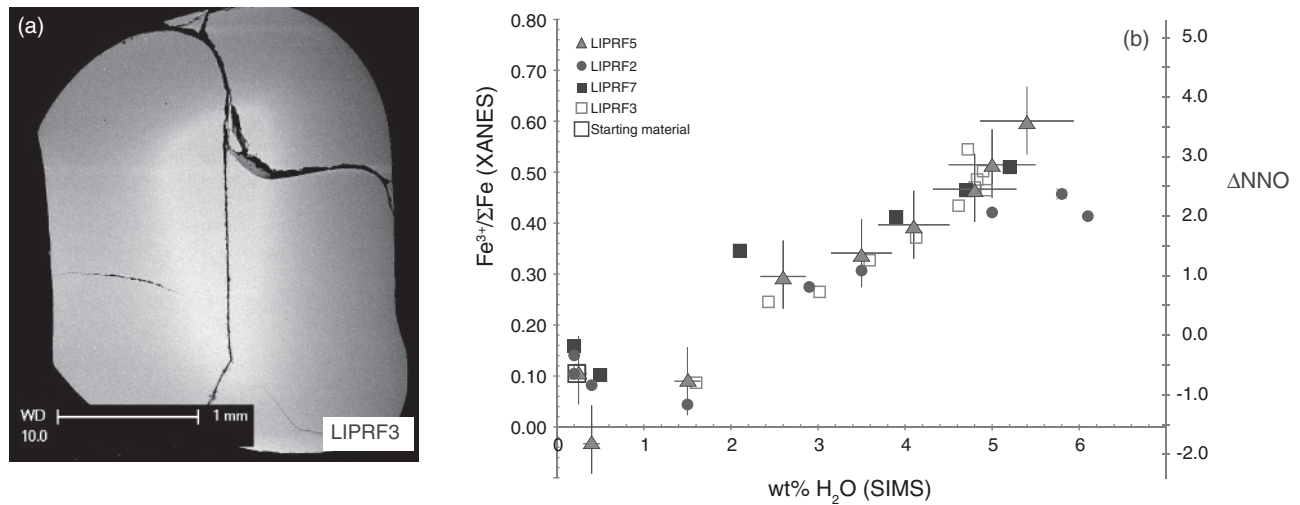
**Fig. 5.** Backscattered electron SEM image showing variation of greyscale intensity related to inward diffusion of $H_2O$ into the Lipari glass chips at high temperature (a), reproduced from Humphreys *et al.* (2008). (b) Co-variation of $Fe^{3+}/\sum Fe$ with $H_2O$ content and equivalent $fO_2$ variation relative to the NNO buffer. Representative error bars shown for sample LIPRF5.
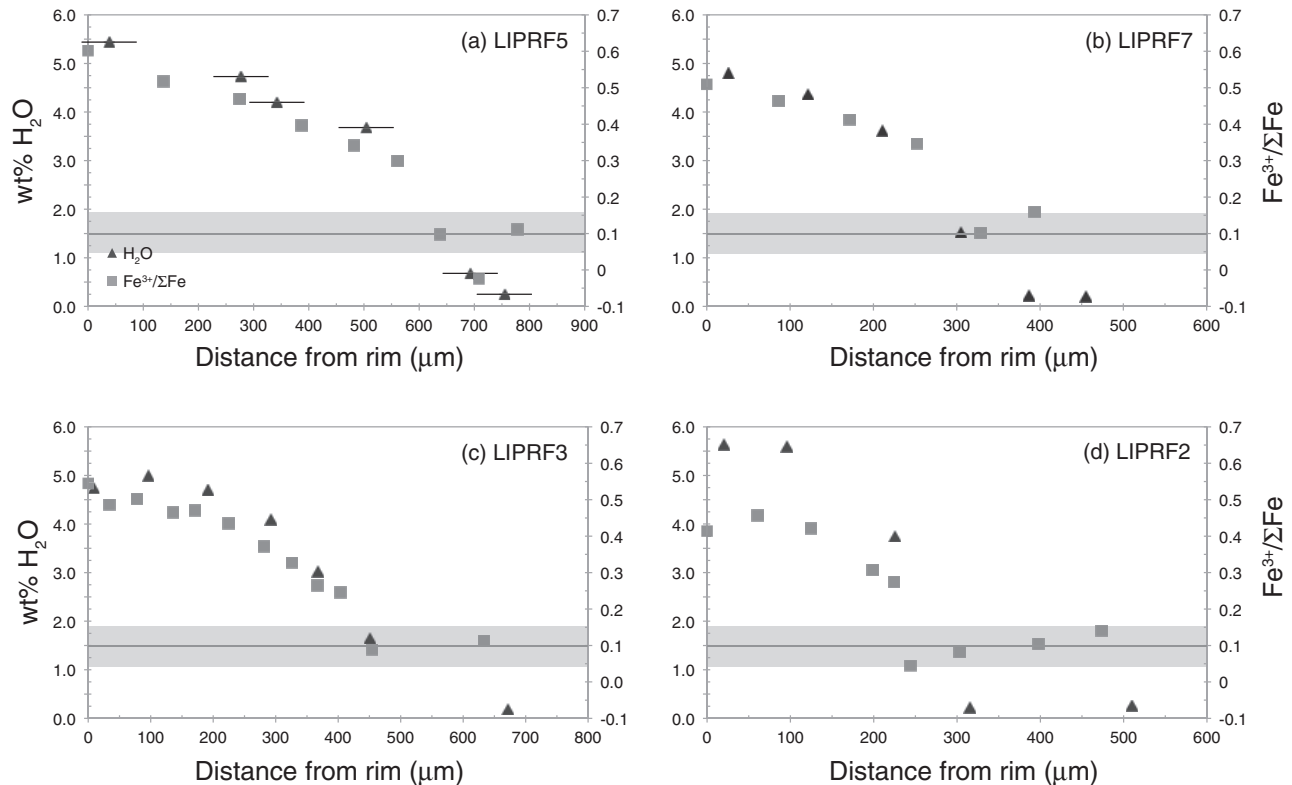


**Fig. 6.** Spatial variability of $Fe^{3+}/\sum Fe$ (grey squares) and $H_2O$ (black triangles) with distance from the rim of each chip hydrated at high temperature. $Fe^{3+}/\sum Fe$ in the unhydrated starting material is marked by a grey band in each figure. Horizontal error bars in (a) are the estimated maximum uncertainty on the spatial location of each point. Errors in $Fe^{3+}/\sum Fe$ and $H_2O$ are reported in previous figures.

sequestration of $H_2$ from the melt, resulting in increased $Fe^{3+}/\sum Fe$ through the reaction

$$H_2(g) + Fe_2O_3(m) = H_2O(m) + 2FeO(m). \quad (10)$$
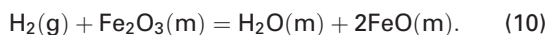
Although the initial $fO_2$ of the melt in these experiments was fairly high, as a result of prolonged equilibration at

high pressure in the cold-seal apparatus (Mangan & Sisson, 2000), this oxidation pattern is consistent with theoretical calculations of increasing oxidation state with degassing for sulphur-free melts (e.g. Mueller, 1971; Candela, 1986; Burgisser & Scaillet, 2007). We used the approach of Burgisser *et al.* (2008) to simulate
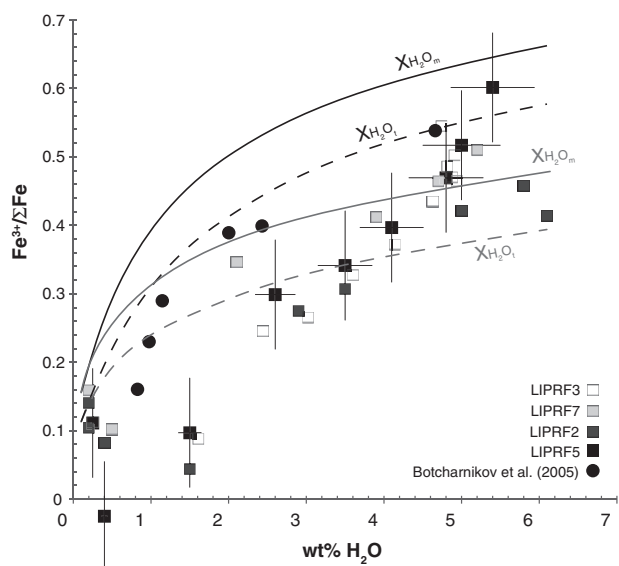
**Fig. 7.** Variation of $Fe^{3+}/\sum Fe$ and $H_2O$ within experimentally hydrated glass chips (squares). Modelled variation of $Fe^{3+}/\sum Fe$ based on changing water activity is shown by the bold lines (calculated from $X H_2 O_m$) and dashed lines (calculated from $X H_2 O_t$). Calculated variations for two illustrative initial $fO_2$ conditions are shown (black and grey lines and labels).

the change in OH partitioning between gas and melt during pressurization in a closed system. Each pressure step results in incremental changes to the species fugacities and their concentrations in the melt, which are calculated using species solubilities, mass balance, and reaction (5). The scale of the observed $fO_2$ increase is somewhat less than that predicted by the model when starting with negligible initial fluid (Fig. 4d). This discrepancy is unlikely to be related to significant changes in $fH_2$ during the course of the experiments, because the decompression run times are very short (17–117 min). Moreover, the experimental apparatus was pressurized by Ar gas, so $H_2$ would tend to migrate out through the capsule, decreasing $fH_2$ and leading to more oxidized conditions. Instead, the following two possibilities are more likely:

1. The modelling does not take into account the buffering capacity of FeO in the melt, which could reduce the absolute increase in oxidation state, particularly at higher initial $fO_2$ (Candela, 1986). However, for a melt with only 1 wt % FeO (as in the case of the Panum Dome rhyolite) this should account for <0·2 log units change in $fO_2$ (Burgisser & Scaillet, 2007).
2. The high proportion of fluid in the experimental capsules is buffering the changes in $fO_2$. The experimental starting materials include ~20 wt% fluid so there is likely to be substantial excess fluid at the beginning of each decompression run. When the modelling is repeated with 10 and 20 wt% initial fluid the scale of the $fO_2$ increase is substantially reduced relative to the run with

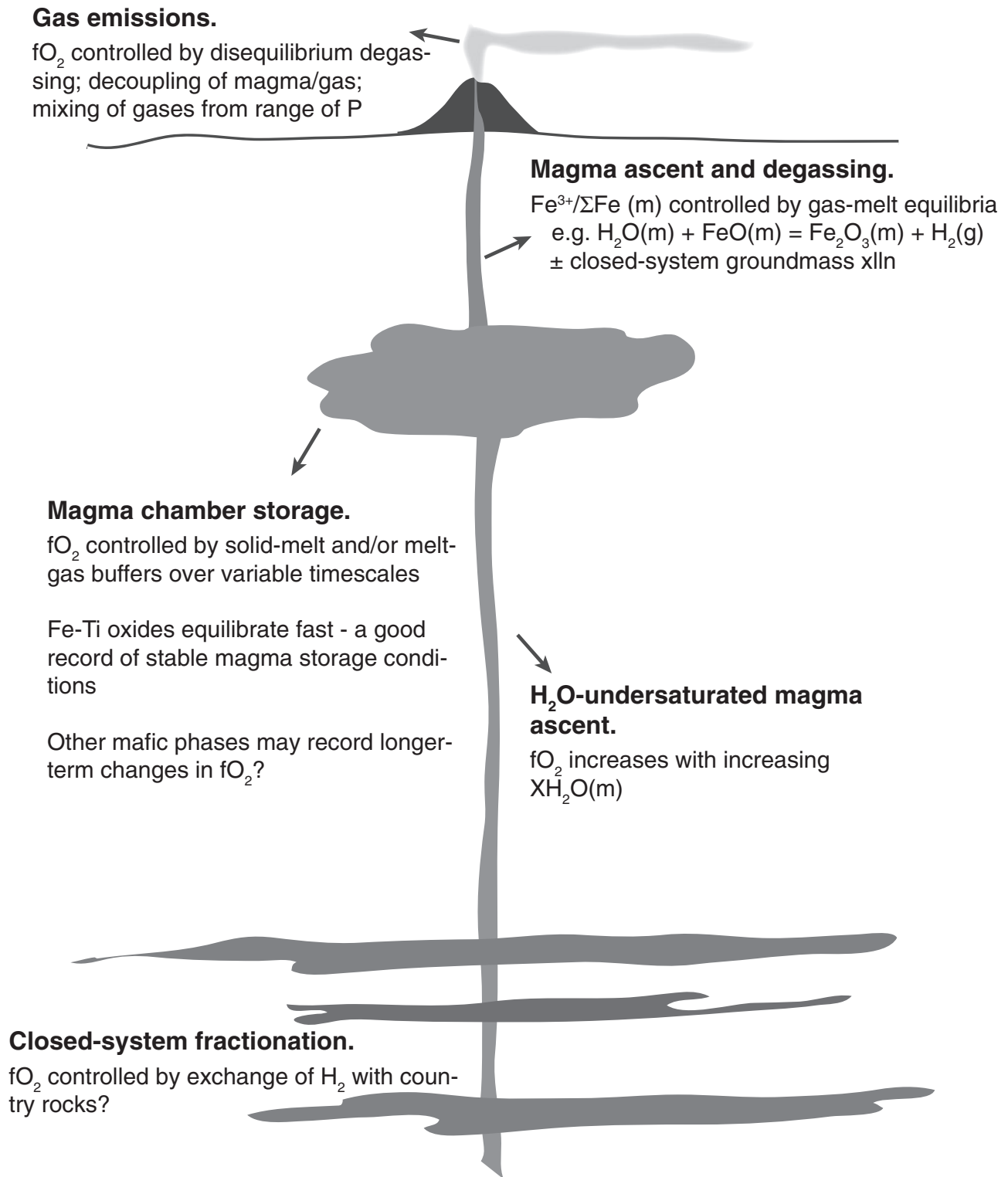0·1 wt% initial fluid (Fig. 4d), to a level consistent with the observations.

The other important difference between the experiments and the modelling is that the experiments were run without equilibration at each pressure step (Mangan & Sisson, 2000); that is, they represent disequilibrium degassing. The disequilibrium arises from delayed bubble nucleation, which is offset to lower pressure than the equilibrium case, but because they were run with a pure $H_2O$ fluid there is no effect on the relationship between $Fe^{3+}/\sum Fe$ and $H_2O$. However, more significant kinetic factors could arise in multi-component fluids with significant differences in volatile species diffusivities. This is highlighted in experiments by Fiege *et al.* (2014) that showed enhanced transfer of sulphur into the fluid relative to the melt at high decompression rates, decreasing to equilibrium values with annealing and producing lower melt $Fe^{3+}/\sum Fe$ than predicted by equilibrium (closed-system) models.

## DISCUSSION

Our data demonstrate that magma degassing and hydration can both result in significant melt oxidation coupled to changes in volatile content. On $H_2O$ saturation, the formation of a free $H_2O$ vapour phase partitions $H_2$ from the melt into the vapour and results in melt oxidation. During hydration, oxidation is caused by changes in water activity. These mechanisms should therefore be considered as one possible way to explain the high oxidation state observed in arc magmas (e.g. Carmichael, 1991). Both processes have direct relevance for crustal processes and may be important in different regions of the arc crust (Fig. 8). Magma ascent from shallow storage regions is dominated by degassing of $H_2O$ vapour from the melt, whereas rise of $H_2O$-undersaturated magma from the deep crust would be associated with increasing water activity. However, arc magmas are complicated by a general lack of equilibrium conditions, instead representing different components or subsystems that may be in equilibrium at different points in the volcanic system. We therefore need to consider what controls $fO_2$ and what phases would record it accurately over varying timescales.

### Degassing in natural systems
Arc magma ascent through a conduit and eruption at the surface is associated with significant volatile degassing (Fig. 8). Our new data and modelling demonstrate that degassing of a pure or dominantly $H_2O$-bearing fluid results in significant melt oxidation. Under closed-system degassing conditions, this can be moderated by the presence of large volumes of gas. Furthermore, the melt can be expected to oxidize even if degassing occurs during disequilibrium degassing (delayed bubble nucleation), provided that the volatile budget is dominated by $H_2O$. In natural systems, we

**Gas emissions.**

$fO_2$ controlled by disequilibrium degassing; decoupling of magma/gas; mixing of gases from range of P

**Magma ascent and degassing.**

$Fe^{3+}/\Sigma Fe$ (m) controlled by gas-melt equilibria
e.g. $H_2O(m) + FeO(m) = Fe_2O_3(m) + H_2(g)$
± closed-system groundmass xlln

**Magma chamber storage.**

$fO_2$ controlled by solid-melt and/or melt-gas buffers over variable timescales

Fe-Ti oxides equilibrate fast - a good record of stable magma storage conditions

Other mafic phases may record longer-term changes in $fO_2$?

**$H_2O$-undersaturated magma ascent.**

$fO_2$ increases with increasing $XH_2O(m)$

**Closed-system fractionation.**

$fO_2$ controlled by exchange of $H_2$ with country rocks?

**Fig. 8.** Schematic depth section showing the possible variations in importance of different $fO_2$ control mechanisms in different parts of a volcanic system and crust, depending on kinetics and degree of equilibration. (See text for discussion.)

would therefore expect to observe a systematic deviation of the oxidation state of the melt from that of the pre-eruptive magma (as measured, for example, by two-oxide equilibria).

Crabtree & Lange (2012) showed that bulk-rock $Fe^{3+}/\sum Fe$ in degassed, crystal-poor andesites from the Mexican volcanic arc was within error of the pre-eruptive $Fe^{3+}/\sum Fe$ of the hydrous melt, as determined by two-oxide thermobarometry. This was interpreted to mean that extensive degassing (of up to 8 wt% $H_2O$) during ascent had no measurable effect on magma oxidation state. Our data indicate that such strong $H_2O$

degassing should leave a clear signature of oxidation in the melt phase. We therefore suggest that the magma may also have degassed additional multivalent gas species (e.g. sulphur) that would counteract the melt oxidation driven by loss of $H_2O$ (Burgisser *et al.*, 2008). Alternatively, the bulk-rock measurements of oxidation state in the degassed magmas may have been insufficiently sensitive to resolve any degassing effects. Direct *in situ* measurements of melt oxidation state (e.g. by XANES) are more likely to resolve these late-stage changes.

Surface volcanic gas emissions represent the counterpart to the continuously degassing melt that is erupted (Fig. 8), but gas $fO_2$ measurements are commonly different from those of their host lavas. This has been interpreted as the result of oxidation state changes to the melt during degassing (e.g. loss of $SO_2$ from basalt, Anderson & Wright, 1972; Helz, 2009) or mixing and integration of multi-component gases released over a range of pressures (Edmonds *et al.*, 2010). In some cases, disequilibrium in the gas phase is evident from lack of correspondence of $fO_2$ estimates using different gas ratios (e.g. $H_2/H_2O$ compared with $CO/CO_2$; Hammouya *et al.*, 1998) and probably results from mixing of gas components with different origins, decoupled from magma ascent (Edmonds *et al.*, 2010). In other cases the gases appear to be in equilibrium with the lavas (e.g. Gerlach, 1993, 2004; Roeder *et al.*, 2003, 2004) and the discrepancy may relate to kinetic differences in the response rate of different redox pairs ($H_2$–$H_2O$ > $SO_2$–$H_2S$ > $CO$–$CO_2$–$CH_4$; Giggenbach, 1996).

These problems indicate that where multiple volatile species are present, the effects of degassing of natural arc magmas on oxidation state are complex, and strongly influenced by temperature, pressure, degassing kinetics and the initial $fO_2$ (Burgisser & Scaillet, 2007; Fiege *et al.*, 2014) as well as the mode of degassing (open system or closed system). This means that analysis of oxidation state during degassing of natural melts is unlikely to yield unique interpretations, although it is clear that arc magma degassing could significantly affect the oxidation state of the melt. Attaining a real understanding of the effects of magmatic degassing on oxidation state will probably require direct measurements of the concentrations and speciation of all major volatiles in the melt, as well as melt $Fe^{3+}/\sum Fe$ and the corresponding gas compositions.

## Magma ascent from the deep crust

Recent models of arc magma genesis involve prolonged periods of deep (mafic) magma intrusion, differentiation and partial melting (e.g. Annen *et al.*, 2006), followed by magma ascent towards upper crustal magma reservoirs where storage, degassing and mingling may also occur (Humphreys *et al.*, 2008; Edmonds *et al.*, 2010; Johnson *et al.*, 2010). Our partial hydration experiments have relevance for the passage of hydrous melts or magmas between the lower crust and shallow magma storage reservoirs (Fig. 8). Although magmas
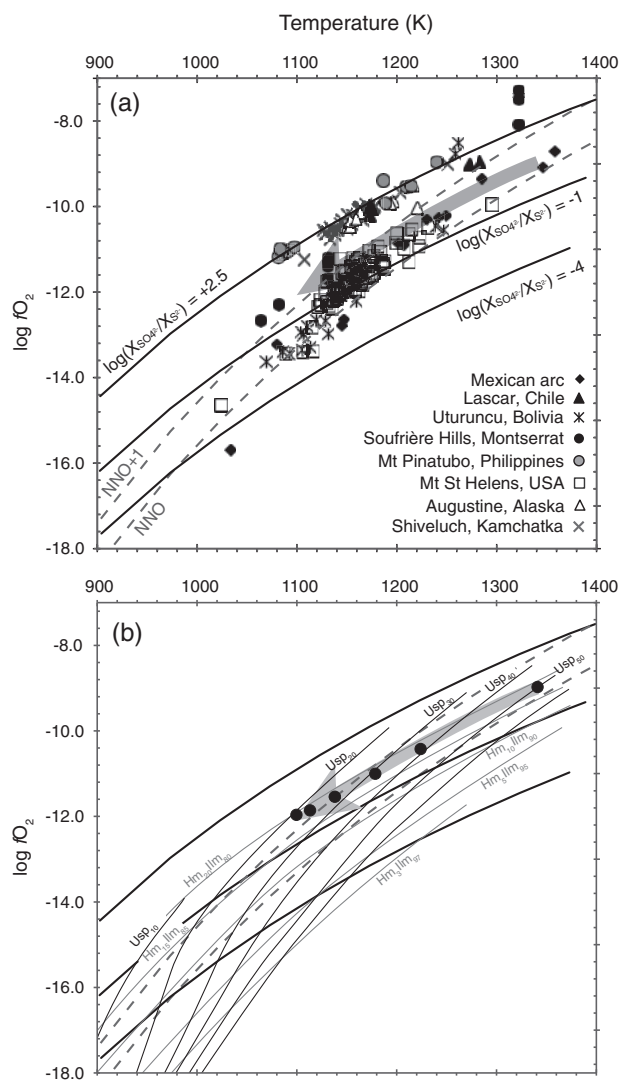


**Fig. 9.** Temperature–$fO_2$ variations in intermediate arc magmas (a). Different oxygen buffers are shown by bold black lines (constant sulphide–sulphate ratios) and grey dashed lines (NNO, NNO + 1). Data points are from two-oxide equilibria. Data sources: Blundy *et al.* (2008) for Mount St Helens, USA; Humphreys *et al.* (2006a) for Shiveluch Volcano, Kamchatka; Roman *et al.* (2006) for Augustine, Aleutians; Crabtree & Lange (2012) for the Mexican arc; Murphy *et al.* (2000) for Soufrière Hills, Montserrat; Sparks *et al.* (2008) for Uturuncu Volcano, Bolivia; Pallister *et al.* (1996) for Mount Pinatubo, Philippines; Matthews *et al.* (1994) for Lascar Volcano, Chile. The grey arrow shows the data trend from (b), which also shows isopleths (thin grey lines) of constant hm–ilm and usp–mt composition from Buddington & Lindsley (1964). Filled black circles in (b) are data for zoned magnetite grains from Soufrière Hills Volcano, Montserrat (from Devine *et al.* 2003), which plot long lines of constant hm–ilm and also lie parallel to constant sulphide–sulphate composition.

originating from the deep crust are thought to be hydrous, they are highly unlikely to be $H_2O$-saturated. This means that melt $aH_2O$ will increase during ascent, as the magma becomes closer to volatile saturation. By analogy with our experimental results, such ascent could result in significant oxidation of the melt under conditions of incomplete diffusive equilibration. Although $H_2O$ diffusion is rapid, we calculate that even

in 10 000 years significant diffusion would be observed over a distance of only ~20 m at 900°C [using the diffusivity model from Nowak & Behrens (1997)]. This means that incomplete equilibration in ascending magmas must be carefully considered as a possible source of $Fe^{3+}/\sum Fe$ heterogeneity. Moreover, this reasoning also suggests that, depending on timescales, magmas in the middle to lower crust could be substantially more reducing than those in the upper levels of magma storage, and hence that crustal-scale variations in $fO_2$ may be possible at subduction zones.

There are already some hints of strong changes in oxidation state during the formation of arc magmas. For example, the cores of a population of plagioclase phenocrysts in intermediate arc magmas were highly anorthitic and corroded, consistent with resorption during $H_2O$-undersaturated magma ascent (Humphreys et al., 2006a). These cores may contain sulphide inclusions, indicating that these plagioclase phenocrysts formed in a more reducing environment than the host magmas, which are typically too oxidizing to have stable sulphides. The presence of Cu–Fe-sulphide inclusions in phenocrysts appears to be a relatively common feature in intermediate arc magmas (e.g. Shiveluch Volcano, Kamchatka; Humphreys et al., 2006a; Santiaguito, Guatemala, Scott et al., 2013; Satsuma-Iwojima, Japan, Ueda & Itaya, 1981; Mount Pinatubo, Philippines, Pallister et al., 1996; Popocatepetl, Mexico, Schaaf et al., 2005), and in their cumulates (Lee et al., 2012). Sulphide crystallization could reflect a stage of fractionation under deep, more reducing, low $aH_2O$ conditions; or alternatively may be coupled to melt redox changes resulting from magnetite crystallization (Carmichael & Ghiorso, 1986; Sun et al., 2004; Jenner et al., 2010), resulting in constant or reducing melt $Fe^{3+}/\sum Fe$ but changing $SO_4^{2-}/S^{2-}$ (Moretti & Papale, 2004; Sun et al., 2004). In any case, these variations in oxidation state could have important implications for the distribution and transport of metals within the arc crust.

## What controls $fO_2$ in magmatic systems?

Although estimates of $fO_2$ for many magmas plot close to solid oxygen buffers (e.g. NNO or QFM), these phases typically do not (co)exist and it is highly unlikely that those solid buffers are controlling magma $fO_2$; instead they are useful reference lines in $T$–$fO_2$ space. However, it has been suggested that gas–melt redox equilibria could actually control magma $fO_2$, if there is abundant free vapour present in the magma. For example, Matthews et al. (1994) suggested that the sulphide–sulphate gas-phase reaction

$$SO_2(g) + H_2O(g) = H_2S(g) + 3/2 O_2(g) \qquad (11)$$
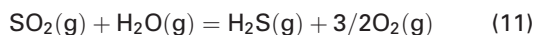
buffered magma $fO_2$ at Lascar Volcano, Chile, leading to more oxidized magmas (relative to the NNO buffer) as temperature decreases. This mechanism would require relatively sulphur-rich gases to be present, although the gas-driven buffer could be very effective

because of its rapid response and large valence change (Matthews et al., 1994). The pattern of increasing divergence from oxide buffers (e.g. $\Delta$NNO) with decreasing temperature, in a trend more parallel to the sulphide–sulphate buffer, is seen at several other volcanoes (Fig. 9a), including Augustine, USA (Roman et al., 2006), Shiveluch, Kamchatka (Humphreys et al., 2006a), Quizapu, Chile (Ruprecht et al., 2012) and Pinatubo (Pallister et al., 1996). Data for Mount St Helens, USA as a whole lie parallel to NNO, but single samples do not (Blundy et al., 2008), instead plotting parallel to the sulphide–sulphate buffer (Fig. 9a).

This suggests that sulphide–sulphate oxygen exchange between the gas and melt might be a common and effective oxygen buffering mechanism for shallowly stored magmas. However, the arrays of $T$–$fO_2$ points from coexisting oxide compositions are also parallel to isopleths of constant hm/ilm (taken from Buddington & Lindsley, 1964; Fig. 9b). Isopleths of constant mt–usp in titanomagnetite are at a slightly steeper angle (Fig. 9b). Therefore, the oxide data could also be explained by increased temperature causing increasing usp content, whereas hm/ilm remains constant. This is consistent with the slower diffusion rates in ilm–hm solid solution than in mt–usp (Hammond & Taylor, 1982). A simpler interpretation for these $T$–$fO_2$ trends is therefore that late-stage heating has resulted in a diffusive increase in the usp content of titanomagnetites, whereas adjustment of ilmenite compositions is kinetically inhibited. The increased temperature could be due to release of latent heat of crystallization (Blundy et al., 2006) or to mingling with hotter magmas (e.g. Devine et al., 2003; Ruprecht et al., 2012). This is consistent with compositional variations in oxides from Soufrière Hills Volcano, Montserrat (Fig. 9b; data from Devine et al., 2003). Ilmenites are uniform, whereas titanomagnetites have zoned rims with high $TiO_2$ owing to magma mixing (Devine et al., 2003). The apparent $T$–$fO_2$ data plot along hm–ilm isopleths and lie parallel to the sulphide–sulphate buffer (Fig. 9b). Demonstrating $fO_2$ control by gas–melt equilibria such as (11) would require evidence of constant melt redox ratios for the redox couple of interest, probably through analysis of suites of melt inclusions.

Disequilibrium between crystals and melt is a ubiquitous feature of shallow crustal arc magma storage: arc magmas typically comprise components or subsystems that may be in equilibrium only at certain points in the volcanic system (e.g. Pichavant et al., 2007). For minerals, equilibration timescales are poorly known but probably slow, except for Fe–Ti oxides, which may equilibrate relatively quickly (i.e. <5 years at 900°C for complete equilibration of a 250 μm oxide phenocryst; Freer & Hauptman, 1978). This means that $fO_2$ calculated from solid–melt equilibria involving homogeneous Fe–Ti oxide phenocrysts ($\pm H_2O$) should be an accurate record (sensor) of stable magma storage conditions in the shallow system. However, oxides will probably not provide a good record of earlier or longer-term changes in $fO_2$

during fractionation, nor of late-stage changes during magma ascent. Instead, more slowly equilibrating phenocrysts such as pyroxene or hornblende, or oxides brought rapidly to the surface in cumulate nodules, may be more useful as a record of longer-term changes; whereas melt redox couples will be needed to investigate variations immediately prior to eruption.

## SUMMARY

Direct measurement of coupled changes in melt $Fe^{3+}/\sum Fe$ and $H_2O$ content in partially hydrated and degassed experimental rhyolites confirms that significant changes in oxidation state can occur in response to changes in volatile content. During hydration, increases in $aH_2O$ produced strong melt oxidation. This suggests that ascent of $H_2O$-undersaturated arc magmas from the deep crust could cause significant oxidation, depending on the timescales required for equilibration relative to magma storage times. During degassing, oxidation arises owing to loss of $H_2$ together with $H_2O$, consistent with theoretical modelling for $H_2O$ fluids. It is therefore possible that significant vertical variations in magma oxidation state may develop within the arc crust. During the fractionation, storage and ascent of natural arc magmas, the controls on $fO_2$ may be expected to vary depending on the nature and duration of magma storage, as well as kinetic factors and the timescales of observation and equilibration. The differing response times of possible oxygen buffers and/or $fO_2$ sensors (such as oxide pairs) need to be considered alongside the degree of attainment of equilibrium in the magma. It is clear that attaining a real understanding of the effects of magmatic degassing on oxidation state will probably require direct measurements of the concentrations and speciation of all major volatiles in the melt, as well as melt $Fe^{3+}/\sum Fe$ and the corresponding gas compositions. In this respect, melt structure and chemistry should be considered alongside variations of $fO_2$ relative to traditional buffers.

## ACKNOWLEDGEMENTS

## FUNDING

## REFERENCES

Anderson, A. T. & Wright, T. L. W. (1972). Phenocrysts and glass inclusions and their bearing on oxidation and mixing of basaltic magmas, Kilauea volcano, Hawaii. *American Mineralogist* **57**, 188–216.

Annen, C., Blundy, J. D. & Sparks, R. S. J. (2006). The genesis of intermediate and silicic magmas in deep crustal hot zones. *Journal of Petrology* **47**, 505–539.

Bajt, S., Sutton, S. R. & Delaney, J. S. (1994). X-ray microprobe analysis of iron oxidation states in silicates and oxides using X-ray absorption near edge structure (XANES). *Geochimica et Cosmochimica Acta* **58**, 5209–5214.

Ballhaus, C. (1993). Redox states of lithospheric and asthenospheric upper mantle. *Contributions to Mineralogy and Petrology* **114**, 331–348.

Berry, A. J., O'Neill, H., Jayasuriya, K. D., Campbell, S. J. & Foran, G. J. (2003). XANES calibrations for the oxidation state of iron in a silicate glass. *American Mineralogist* **88**, 967–977.

Blundy, J. & Cashman, K. (2005). Rapid decompression-driven crystallization recorded by melt inclusions from Mount St Helens volcano. *Geology* **33**, 793–796.

Blundy, J., Cashman, K. & Humphreys, M. (2006). Magma heating by decompression-driven crystallization beneath andesite volcanoes. *Nature* **443**, 76–80.

Blundy, J., Cashman, K. V. & Berlo, K. (2008). Evolving magma storage conditions beneath Mount St Helens inferred from chemical variations in melt inclusions from the 1980–1986 and current (2004–2006) eruptions. In: Sherrod, D. R., Scott, W. E. and Stauffer, P. H. (eds) *A volcano rekindled: The renewed eruption of Mount St. Helens, 2004–2006. US Geological Survey Professional Paper* **1750**, 755–790.

Botcharnikov, R. E., Koepke, J., Holtz, F., McCammon, C. & Wilke, M. (2005). The effect of water activity on the oxidation and structural state of Fe in a ferro-basaltic melt. *Geochimica et Cosmochimica Acta* **69**, 5071–5085.

Brandon, A. D. & Draper, D. S. (1996). Constraints on the origin of the oxidation state of mantle overlying subduction zones: An example from Simcoe, Washington, USA. *Geochimica et Cosmochimica Acta* **60**, 1739–1749.

Brooker, R. A., Kohn, S. C., Holloway, J. R., McMillan, P. F. & Carroll, M. R. (1999). Solubility, speciation and dissolution mechanisms for $CO_2$ in melts on the $NaAlO_2$–$SiO_2$ join. *Geochimica et Cosmochimica Acta* **63**, 3549–3565.

Buddington, A. F. & Lindsley, D. H. (1964). Iron–titanium oxide minerals and synthetic equivalents. *Journal of Petrology* **5**, 310–357.

Burgisser, A. & Scaillet, B. (2007). Redox evolution of a degassing magma rising to the surface. *Nature* **445**, 194–197.

Burgisser, A., Scaillet, B. & Harshvardhan (2008). Chemical patterns of erupting silicic magmas and their influence on the amount of degassing during ascent. *Journal of Geophysical Research* **113**, B12204.

Burnham, C. W. (1975). Water and magmas; a mixing model. *Geochimica et Cosmochimica Acta* **39**, 1077–1084.

Candela, P. A. (1986). The evolution of aqueous vapor from silicate melts: Effect on oxygen fugacity. *Geochimica et Cosmochimica Acta* **50**, 1205–1211.

Carmichael, I. S. E. (1991). The redox states of basic and silicic magmas: a reflection of their source regions? *Contributions to Mineralogy and Petrology* **106**, 129–141.

Carmichael, I. S. E. & Ghiorso, M. S. (1986). Oxidation–reduction relations in basic magma: a case for homogeneous equilibria. *Earth and Planetary Science Letters* **78**, 200–210.

Chou, I. M. (1986). Permeability of precious metals to hydrogen at 2 kb total pressure and elevated temperatures. *American Journal of Science* **286**, 638–658.

Cottrell, E., Kelley, K. A., Lanzirotti, A. & Fischer, R. A. (2009). High-precision determination of iron oxidation state in silicate glasses using XANES. *Chemical Geology* **268**, 167–179.

Crabtree, S. M. & Lange, R. A. (2012). An evaluation of the effect of degassing on the oxidation state of hydrous andesite and dacite magmas: a comparison of pre- and post-eruptive $Fe^{2+}$ concentrations. *Contributions to Mineralogy and Petrology* **163**, 209–224.

Devine, J. D., Rutherford, M. J., Norton, G. E. & Young, S. R. (2003). Magma storage region processes inferred from geochemistry of Fe–Ti oxides in andesitic magma, Soufrière Hills Volcano, Montserrat, W.I. *Journal of Petrology* **44**, 1375–1400.

Duffy, J. A. (1993). A review of optical basicity and its applications to oxidic systems. *Geochimica et Cosmochimica Acta* **57**, 3961–3970.

Edmonds, M., Aiuppa, A., Humphreys, M., Moretti, R., Giudice, G., Martin, R. S., Herd, R. A. & Christopher, T. (2010). Excess volatiles supplied by mingling of mafic magma at an andesite arc volcano. *Geochemistry, Geophysics, Geosystems* **11**, Q04005.

Evans, K. A., Elburg, M. A. & Kamenetsky, V. S. (2012). Oxidation state of subarc mantle. *Geology* **40**, 783.

Fiege, A., Behrens, H., Holtz, F. & Adams, F. (2014). Kinetic vs. thermodynamic control of degassing of $H_2O$–S ± Cl-bearing andesitic melts. *Geochimica et Cosmochimica Acta* **125**, 241–264.

Flood, H. & Förland, T. (1947). The acidic and basic properties of oxides. *Acta Chemica Scandinavica* **1**, 592–604.

Fraser, D. G. (1975). Activities of trace elements in silicate melts. *Geochimica et Cosmochimica Acta* **39**, 1525–1530.

Fraser, D. G. (1977). Thermodynamic properties of silicate melts. In: Fraser, D. G. (ed.) *Thermodynamics in Geology*. Dordrecht: D. Reidel, pp. 303–325.

Fraser, D. G. (2005). Acid–base properties and structons: towards a structural model for predicting the thermodynamic properties of silicate melts. *Annals of Geophysics* **48**, 549–559.

Freer, R. & Hauptman, Z. (1978). An experimental study of magnetite–titanomagnetite interdiffusion. *Physics of the Earth and Planetary Interiors* **16**, 223–231.

Frost, D. J. & McCammon, C. A. (2008). The redox state of Earth's mantle. *Annual Review of Earth and Planetary Sciences* **36**, 389–420.

Gaillard, F., Scaillet, B., Pichavant, M. & Bény, J.-M. (2001). The effect of water and $fO_2$ on the ferric–ferrous ratio of silicic melts. *Chemical Geology* **174**, 255–273.

Gaillard, F., Scaillet, B. & Pichavant, M. (2002). Kinetics of iron oxidation–reduction in hydrous silicic melts. *American Mineralogist* **87**, 829–837.

Gaillard, F., Pichavant, M., Mackwell, S., Champallier, R., Scaillet, B. & McCammon, C. (2003a). Chemical transfer during redox exchanges between $H_2$ and Fe-bearing silicate melts. *American Mineralogist* **88**, 308–315.

Gaillard, F., Pichavant, M. & Scaillet, B. (2003b). Experimental determination of activities of FeO and $Fe_2O_3$ components in hydrous silicic melts under oxidising conditions. *Geochimica et Cosmochimica Acta* **67**, 4389–4409.

Gaillard, F., Schmidt, B., Mackwell, S. & McCammon, C. (2003c). Rate of hydrogen–iron redox exchange in silicate melts and glasses. *Geochimica et Cosmochimica Acta* **67**, 2427–2441.

Gerlach, T. M. (1993). Oxygen buffering of Kilauea volcanic gases and the oxygen fugacity of Kilauea basalt. *Geochimica et Cosmochimica Acta* **57**, 795–814.

Gerlach, T. M. (2004). Comment on paper: 'Morphology and compositions of spinel in Pu'u 'O'o lava (1996–1998), Kilauea volcano, Hawaii'—enigmatic discrepancies between lava and gas-based $fO_2$ determinations of Pu'u 'O'o lava. *Journal of Volcanology and Geothermal Research* **134**, 241–244.

Giggenbach, W. F. (1996). Redox processes governing the chemistry of fumarolic gas discharges from White Island, New Zealand. *Applied Geochemistry* **2**, 143–161.

Hammond, P. A. & Taylor, L. A. (1982). The ilmenite/titano-magnetite assemblage: kinetics of re-equilibration. *Earth and Planetary Science Letters* **61**, 143–150.

Hammouya, G., Allard, P., Jean-Baptiste, P., Parello, F., Semet, M. P. & Young, S. R. (1998). Pre- and syn-eruptive geochemistry of volcanic gases from Soufrière Hills of Montserrat, West Indies. *Geophysical Research Letters* **25**, 3685–3688.

Helz, R. T. (2009). Reduction of basaltic melt during near-surface evolution of $SO_2$: A possible example from Kilaeua. Portland GSA Annual Meeting, 2009, 248–21.

Humphreys, M. C. S., Blundy, J. D. & Sparks, R. S. J. (2006a). Magma evolution and open-system processes at Shiveluch Volcano: Insights from phenocryst zoning. *Journal of Petrology* **47**, 2303–2334.

Humphreys, M. C. S., Kearns, S. L. & Blundy, J. D. (2006b). SIMS investigation of electron-beam damage to hydrous, rhyolitic glasses: Implications for melt inclusion analysis. *American Mineralogist* **91**, 667–679.

Humphreys, M. C. S., Menand, T., Blundy, J. D. & Klimm, K. (2008). Magma ascent rates in explosive eruptions: constraints from $H_2O$ diffusion in melt inclusions. *Earth and Planetary Science Letters* **270**, 25–40.

Jenner, F. E., O'Neill, H. St. C., Arculus, R. J. & Mavrogenes, J. A. (2010). The magnetite crisis in the evolution of arc-related magmas and the initial concentration of Au, Ag and Cu. *Journal of Petrology* **51**, 2445–2464.

Johnson, E. R., Wallace, P. J., Cashman, K. V. & Delgado Granados, H. (2010). Degassing of volatiles ($H_2O$, $CO_2$, S, Cl) during ascent, crystallization and eruption at mafic monogenetic volcanoes in central Mexico. *Journal of Volcanology and Geothermal Research* **197**, 225–238.

Kelley, K. A. & Cottrell, E. (2009). Water and the oxidation state of subduction zone magmas. *Science* **325**, 605–607.

Kohn, S. C. (2000). The dissolution mechanisms of water in silicate melts; a synthesis of recent data. *Mineralogical Magazine* **64**, 389–408.

Kress V. C. & Carmichael, I. S. E. (1991). The compressibility of silicate liquids containing $Fe_2O_3$ and the effect of composition, temperature, oxygen fugacity and pressure on their redox states. *Contributions to Mineralogy and Petrology* **108**, 82–92.

Kushiro, I. (1975). On the nature of silicate melt and its significance in magma genesis: regularities in the shift of the liquidus boundaries involving olivine, pyroxene, and silica minerals. *American Journal of Science* **275**, 411–431.

Lecuyer, C. & Ricard, Y. (1999). Long-term fluxes and budget of ferric iron: implication for the redox states of the Earth's mantle and atmosphere. *Earth and Planetary Science Letters* **165**, 197–211.

Lee, C.-T. A., Luffi, P., Le Roux, V., Dasgupta, R., Albarède, F. & Leeman, W. P. (2010). The redox state of arc mantle using Zn/Fe systematics. *Nature* **468**, 681–685.

Lee, C.-T. A., Luffi, P., Chin, E. J., Bouchet, R., Dasgupta, R., Morton, D. M., Le Roux, V., Yin, Q. & Jin, D. (2012). Copper systematics in arc magmas and implications for crust–mantle differentiation. *Science* **336**, 64–68.

Malfait, W. J. (2014). The nearly complete dissociation of water in glasses with strong aluminum avoidance. *American Mineralogist* **99**, 1648–1652.

Mallman, G. & O'Neill, H. (2009). The crystal/melt partitioning of V during mantle melting as a function of oxygen fugacity compared with some other elements (Al, P, Ca, Sc, Ti, Cr, Fe, Ga, Y, Zr and Nb). *Journal of Petrology* **50**, 1765–1794.

Mangan, M. & Sisson, T. (2000). Delayed, disequilibrium degassing in rhyolite magma: decompression experiments and implications for explosive volcanism. *Earth and Planetary Science Letters* **183**, 441–455.

Mathez, E. A. (1984). Influence of degassing on oxidation states of basaltic magmas. *Nature* **310**, 371–375.

Matthews, S. J., Jones, A. P. & Beard, A. D. (1994). Buffering of melt oxygen fugacity by sulphur redox reactions in calc-alkaline magmas. *Journal of the Geological Society, London* **151**, 815–823.

Moore, G., Righter, K. & Carmichael, I. S. E. (1995). The effect of dissolved water on the oxidation state of iron in natural silicate liquids. *Contributions to Mineralogy and Petrology* **120**, 170–179.

Moretti, R. (2005). Polymerisation, basicity, oxidation state and their role in ionic modelling of silicate melts. *Annals of Geophysics* **48**, 583–608.

Moretti, R. & Papale, P. (2004). On the oxidation state and volatile behaviour in multicomponent gas–melt equilibria. *Chemical Geology* **213**, 265–280.

Morris, R. V. & Haskin, L. A. (1974). EPR measurement of the effect of glass composition on the oxidation states of europium. *Geochimica et Cosmochimica Acta* **38**, 1435–1445.

Mueller, R. F. (1971). Oxidative capacity of magmatic components. *American Journal of Science* **270**, 236–243.

Murphy, M. D., Sparks, R. S. J., Barclay, J., Carroll, M. R. & Brewer, T. S. (2000). Remobilization of andesite magma by intrusion of mafic magma at the Soufriere Hills Volcano, Montserrat, West Indies. *Journal of Petrology* **41**, 21–42.

Mysen, B. O., Kumamoto, K., Cody, G. D. & Fogel, M. L. (2011). Solubility and solution mechanisms of C–O–H volatiles in silicate melt with variable redox conditions and melt composition at upper mantle temperatures and pressures. *Geochimica et Cosmochimica Acta* **75**, 6183–6199.

Nowak, M. & Behrens, H. (1997). An experimental investigation on diffusion of water in haplogranitic melts. *Contributions to Mineralogy and Petrology* **126**, 365–376.

Ottonello, G., Moretti, R., Marini, L. & Vetuschi Zuccolini, M. (2001). Oxidation state of iron in silicate glasses and melts: a thermochemical model. *Chemical Geology* **174**, 157–179.

Pallister, J. S., Hoblitt, R. P., Meeker, G. P., Knight, R. J. & Siems, D. F. (1996). Magma mixing at Mount Pinatubo: Petrographic and chemical evidence from the 1991 deposits. In: Newhall, C. G. & Punongbayan, R. S. (eds) *Fire and Mud: Eruptions and Lahars of Mount Pinatubo, Philippines* p. 687–732.

Parkinson, I. J. & Arculus, R. J. (1999). The redox state of subduction zones: insights from arc-peridotites. *Chemical Geology* **160**, 409–423.

Paul, A. & Douglas, R. W. (1965). Ferrous–ferric equilibrium in binary alkali silicate glasses. *Physics and Chemistry of Glasses* **6**, 207–211.

Pichavant, M., Costa, F., Burgisser, A., Scaillet, B., Martel, C. & Poussineau, S. (2007) Equilibration scales in silicic to intermediate magmas – implications for experimental studies. *Journal of Petrology* **48**, 1955–1972.

Ravel, B. & Newville, M. (2005). ATHENA, ARTEMIS, HEPHAESTUS: data analysis for X-ray absorption spectroscopy using IFEFFIT. *Journal of Synchrotron Radiation* **12**, 537–541.

Roeder, P. L., Thornber, C., Poustovetov, A. & Grant, A. (2003). Morphology and composition of spinel in Pu'u O'o lava (1996–1998), Kilauea volcano, Hawaii. *Journal of Volcanology and Geothermal Research* **123**, 245–265.

Roeder, P. L., Thornber, C. & Grant, A. (2004). Reply to comment on paper: 'Morphology and composition of spinel in Pu'u O'o lava (1996–1998), Kilauea volcano, Hawaii'—enigmatic discrepancies between lava and gas-based $fO_2$ determinations of Pu'u O'o lava. *Journal of Volcanology and Geothermal Research* **134**, 245–248.

Roman, D. C., Cashman, K. V., Gardner, C. A., Wallace, P. J. & Donovan, J. J. (2006). Storage and interaction of compositionally heterogeneous magmas from the 1986 eruption of Augustine Volcano, *Alaska. Bulletin of Volcanology*, 68, 240–254.

Ruprecht, P., Bergantz, G. W., Cooper, K. M. & Hildreth, W. (2012). The crustal magma storage system of Volcàn Quizapu, Chile, and the effects of magma mixing on magma diversity. *Journal of Petrology* **53**, 801–840.

Sack, R. O., Carmichael, I. S. E., Rivers, M. & Ghiorso, M. S. (1980). Ferric–ferrous equilibria in natural silicate liquids at 1 bar. *Contributions to Mineralogy and Petrology* **75**, 369–376.

Sato, M. (1978). Oxygen fugacity of basaltic magmas and the role of gas-forming elements. *Geophysical Research Letters* **5**, 447–449.

Schaaf, P., Stimac, J., Siebe, C. & Macias, J. L. (2005). Geochemical evidence for mantle origin and crustal processes in volcanic rocks from Popocatépetl and surrounding monogenetic volcanoes, Central Mexico.

Schuessler, J. A., Botcharnikov, R. E., Behrens, H., Misiti, V. & Freda, C. (2008). Oxidation state of iron in hydrous phono-tephritic melts. *American Mineralogist* **93**, 1493–1504.

Scott, J. A. J., Pyle, D. M., Mather, T. A. & Rose, W. I. (2013). Geochemistry and evolution of the Santiaguito volcanic dome complex, Guatemala. *Journal of Volcanology and Geothermal Research* **252**, 92–107.

Silver, L., Ihinger, P. D. & Stolper, E. (1990). The influence of bulk composition on the speciation of water in silicate glasses. *Contributions to Mineralogy and Petrology* **104**, 142–162.

Sisson, T. W. & Grove, T. L. (1993). Experimental investigations of the role of $H_2O$ in calc-alkaline differentiation and subduction zone magmatism. *Contributions to Mineralogy and Petrology* **113**, 143–166.

Sparks, R. S. J., Folkes, C. B., Humphreys, M. C. S., Barfod, D. N., Clavero, J., Sunagua, M. C., McNutt, S. R. & Pritchard, M. E. (2008). Uturuncu Volcano, Bolivia: Volcanic unrest due to mid-crustal magma intrusion. *Journal of Science* **308**, 727–769.

Stolper, E. (1982). The speciation of water in silicate melts. *Geochimica et Cosmochimica Acta* **46**, 2609–2620.

Sun, W., Arculus, R. J., Kamenetsky, V. S. & Binns, R. A. (2004). Release of gold-bearing fluids in convergent margin magmas prompted by magnetite crystallization. *Nature* **431**, 975–978.

Tilquin, J.-Y., Duveiller, P., Glibert, J. & Claes, P. (1997). Effect of basicity on redox equilibria in sodium silicate melts: An *in*

*situ* electrochemical investigation. *Journal of Non-Crystalline Solids* **211**, 95–104.

Toop, G. W. & Samis, C. S. (1962). Activities of ions in silicate melt. *Transactions of the Metallurgical Society* **224**, 878–887.

Toplis, M. J. (2005). The thermodynamics of iron and magnesium partitioning between olivine and liquid: criteria for assessing and predicting equilibrium in natural and experimental systems. *Contributions to Mineralogy and Petrology* **149**, 22–39.

Ueda, A. & Itaya, T. (1981). Microphenocrystic pyrrhotite from dacite rocks of Satsuma-Iwojima, Southwest Kyushu, Japan and the solubility of sulfur in dacite magma. *Contributions to Mineralogy and Petrology* **78**, 21–26.

Wilke, M., Farges, F., Petit, P.-E., Brown, G. E. & Martin, F. (2001). Oxidation state and coordination of Fe in minerals: An Fe K-XANES spectroscopic study. *American Mineralogist* **86**, 714–730.

Wilke, M., Partzsch, G. M., Bernhardt, R. & Lattard, D. (2005). Determination of the iron oxidation state in basaltic glasses using XANES at the K-edge. *Chemical Geology* **220**, 143–161.

Wood, B. J., Bryndzia, L. T. & Johnson, K. E. (1990). Mantle oxidation state and its relationship to tectonic environment and fluid speciation. *Science* **248**, 337–345.

Xue, X. & Kanzaki, M. (2004). Dissolution mechanisms of water in depolymerized silicate melts: Constraints from $^{1}$H and $^{29}$Si NMR spectroscopy and *ab initio* calculations. *Geochimica et Cosmochimica Acta* **68**, 5027–5057.

Xue, X. & Kanzaki, M. (2006). Depolymerization effect of water in aluminosilicate glasses: Direct evidence from $^{1}$H–$^{27}$Al heteronuclear correlation NMR. *American Mineralogist* **91**, 1922–1926.

Yokokawa, T. (1986). Gas solubilities in molten salts and silicates. *Pure and Applied Chemistry* **58**, 1547–1552.

Zhang, Y. & Behrens, H. (2000). $H_2O$ diffusion in rhyolitic melts and glasses. *Chemical Geology* **169**, 243–262.

Zhang, Y., Stolper, E. M. & Wasserburg, G. J. (1991). Diffusion of water in rhyolitic glasses. *Geochimica et Cosmochimica Acta* **55**, 441–456.